Electronic structure and magnetic properties of $Sr_2CrReO_6/BaTiO_3$ hybrid heterostructures

V. N. Antonov,[1,2,3] S. Uba,[2] L. Uba,[2] L. V. Bekenov,[1] and A. Bonda[2]

[1]*G. V. Kurdyumov Institute for Metal Physics of the N.A.S. of Ukraine, 36 Vernadsky Street, 03142 Kiev, Ukraine*

[2]*Faculty of Mathematics and Informatics, University of Bialystok, K. Ciolkowskiego 1M, PL-15-245 Bialystok, Poland*

[3]*Max-Planck Institut für Mikrostrukturphysik, Weinberg 2, D-06120 Halle, Germany*

(Received 25 April 2018; revised manuscript received 31 July 2018; published 15 August 2018)

We report on the electronic structure and magnetic properties of hybrid heterostructures of the ferromagnetic double perovskite Sr_2CrReO_6 (SCRO) and ferroelectric $BaTiO_3$ (BTO) calculated in the GGA approach using the fully relativistic spin-polarized Dirac LMTO method. The electronic band structure and optical properties are studied in the BTO and SCRO oxides as well as in SCRO/BTO heterostructures with different supercells: SCRO/BTO monolayered $(1 \times 1 \times 1)$, $(2 \times 2 \times 1)$, and $(1 \times 1 \times 2)$ heterostructures. We investigated theoretically the magnetization, spin and orbital magnetic moments as well as magnetocrystalline anisotropy energy (MAE) in the SCRO on the BTO substrate as a function of the temperature assuming that the finite temperature can be mimicked by the experimental lattice constants corresponding to this temperature. We found that the spin and orbital magnetic moments are monotonic, almost linear functions of temperature but change abruptly at the points of the BTO structural phase transitions. The magnetization M also possesses "jumps" at the structural phase transitions in agreement with the experiment. However, the theoretically predicted jumps in the total magnetic moment are much smaller than the experimentally measured ones. We found that the Cr/Re disorder increases the jump in the magnetic moment by an order of magnitude compared to the calculated data without disorder. The microscopic origin of such huge effect is discussed. The theoretically calculated temperature dependence of the total magnetic moment with 25% of the Cr/Re disorder is in excellent agreement with the critical amplitude, obtained from the fitting of the experimentally measured magnetization $M(T)$. From the theoretically calculated MAE we found that the easy axis of magnetization for the tetragonal and orthorhombic phases is along the $\langle 001 \rangle$ direction in agreement with the experiment. However, it changes to the $\langle 11\bar{1} \rangle$ direction in the rhombohedral phase. The intersite Cr/Re disorder reduces the MAE for the tetragonal and orthorhombic phases and increases it for the rhombohedral phase. We found that the major contribution to the MAE is due to the orbital magnetic anisotropy at the Re site. We also found that the MAE in the monolayered SCRO/BTO heterostructure is significantly increased in comparison with the MAE in SCRO on BTO substrate. The element-specific x-ray absorption spectra as well as the x-ray magnetic circular dichroism at the Ti, Ba, and Re $L_{2,3}$ edges in SCRO/BTO heterostructures are investigated theoretically from first principles and compared with available experimental spectra.

DOI: 10.1103/PhysRevB.98.064414

I. INTRODUCTION

Materials with multiple simultaneous electric and magnetic ordering offer possibilities for new physical cross-correlation effects and therefore new concepts for applications. Ferroelectricity and ferromagnetism derive from the fact that the electrons possess charge and spin. Depending on the surroundings, a material may have an electric polarization or a magnetic polarization. A few materials possess both ferroelectric and magnetic polarizations in the same phase and a coupling between them. These materials are called multiferroics and possess the so-called magnetoelectric (ME) effect, meaning magnetic (electric) induction of polarization P (magnetization M) [1,2]. Multiferroics offer rich physics and novel device concepts, which have recently become of great interest to researchers [3–6]. Aside from the potential applications, the fundamental physics of multiferroic materials is rich and fascinating.

However, only a small number of multiferroics offer a perspective for applications. A key reason for this limited set is the fact that the two order parameters have exactly opposite requirements in terms of the electronic structure. Typically, ferromagnetism (especially in metallic systems) is related to the ordering of spins of electrons in incomplete ionic shells, that is, it results from partially filled d orbitals and requires the kinetic energy of the electron to be dominant; on the other hand, ferroelectricity results from relative shifts of negative and positive ions that induce surface charges, usually it requires formally empty d orbitals and a perfectly insulating state. For this reason, in a single-phase multiferroic, the effect is often very weak, and multiple ordering occurs only at low temperatures for most materials. As a result, potential applications have not been realized yet. In fact, $BiFeO_3$ is the only room temperature multiferroic (antiferromagnetic and ferroelectric) so far, which has attracted great interest and extensive studies in the past decade [7].

In parallel to extensive research on synthesizing single-phase multiferroics and exploring relevant magnetoelectric phenomena, much effort has been made to synthesize heterostructure thin films composed of materials that have large ferromagnetic (FM) and ferroelectric (FE) ordering, with the possibility of ME coupling. Several configurations have been

 ©2018 American Physical Society

employed to fabricate ME composite thin films: composites with FE or FM terminal layers, multilayer nanostructures, superlattice structures with alternate FM and FE layers, and epitaxial ferroelectromagnetic nanocomposites fabricated by self-assembly technique. These nanostructured thin films have been found to exhibit a larger ME effect than that of the single-phase materials by more than one order of magnitude [8]. A new level in design and development in multiferroic thin films has been achieved due to improved first-principles computational techniques. The advancement of both experimental fabrication processes and theoretical modeling codes and parallel processing among theoretical and experimental scientists has aided in the design of new magnetoelectrics with larger coupling parameters [9,10].

Most technologically important ferroelectrics such as $BaTiO_3$ (BTO) and $(Pb, Zr)TiO_3$ are transition metal oxides with perovskite (ABO_3) structure. They have a cubic structure at high temperature with a small B-site cation at the center of an octahedral cage of oxygen ions and a large A-site cation at the unit cell corners. In parallel, there is a large number of ferrites with a spinel structure (AB_2O_4) [11]. Recently, there have been reports on $CoFe_2O_4/BaTiO_3$, $SrRuO_3/BaTiO_3$, $La_{0.67}Sr_{0.33}MnO_3/BaTiO_3$, and $Fe_3O_4/BaTiO_3$ hybrids [12–17]. They show a magnetoelectric coupling effect, manifesting itself as a change in the magnetization and resistance of the ferromagnetic thin film at the structural phase transition temperatures of $BaTiO_3$.

In this regard, another group of promising materials are the ferromagnetic double perovskites (DP) $A_2BB'O_6$ (A = alkaline earth or rare earth and BB′ are heterovalent transition metals such as B = Fe, Cr, Mn, Co, Ni; B′ = Mo, Re, W) [18,19]. They often demonstrate intrinsically complex magnetic structures and a wide variety of physical properties as a consequence of the strong interplay between structure, charge, and spin ordering [20] (see Ref. [21] for a review paper on these materials). In particular, the series $Sr_2CrB'O_6$ with B′ being W, Re, or Os ions is very promising due to their record high values of T_c (T_c = 500 and 635 K for B′ = W and Re, respectively) [22,23]. Sr_2CrOsO_6 has an even higher ordering temperature T_c = 725 K, the highest known in this class, and was reported to be an insulator [24].

Czeschka *et al.* [25] and Opel *et al.* [26] have grown heteroepitaxial Sr_2CrReO_6 (SCRO) on BTO by laser-MBE. Due to coherent growth, the in-plane lattice constants and crystal structure type of the SCRO film follow those of the BTO substrate as a function of temperature. In particular, the epitaxial coherency strain in the SCRO film abruptly changes at the structural phase transitions of BTO. The magnetization of the ferromagnetic SCRO film together with its resistivity shows large steplike variations at the corresponding phase transition temperatures. This demonstrates a strong coupling of the magnetic properties to elastic distortions, i.e., a large magnetoelastic coupling. Taken together, a strong coupling between the ferroelectric order parameter in BTO and the ferromagnetic order parameter in SCRO has been shown. Hence the SCRO/BTO heterostructure can be considered as a magnetoelectric multiferroic.

Artificial oxide heterostructures are particularly promising for the realization of materials with improved and new functionalities and novel device concepts. Nanostructuring is a promising approach that has opened the door to the design of practical devices based on ME coupling. Thin film multiferroics are beginning to reveal a range of fascinating phenomena as well as to stimulate the exploration of new device heterostructures, which have potential applications in microdevices and integrated units such as microsensors, microelectromechanical system (MEMS) devices, and high density information storage. Hereby, interface and surface effects play a crucial role. Due to the complexity of the involved oxide materials, the rich variety of physics resulting from band bending effects, magnetic exchange, or elastic coupling at interfaces in heterostructures is far from being understood and needs further detailed studies. Moreover, intermixing of the different atomic species deposited in multilayer structures plays an important role and might influence or even dominate the overall physical properties. Therefore a careful investigation of the electronic structure of artificial material systems is highly necessary.

The aim of this work is to preform a detailed theoretical investigation of the electronic structure, optical properties, and x-ray magnetic circular dichroism (XMCD) in SCRO/BTO heterostructures. The energy band structure of these heterostructures is calculated within the *ab initio* approach using the fully relativistic spin-polarized Dirac LMTO method. We also investigated the temperature dependence of the magnetization, spin, and orbital magnetic moments, as well as the magnetocrystalline anisotropy energy (MAE) in the SCRO on the BTO substrate.

The paper is organized as follows. The computational details are presented in Sec. II. Section III presents the electronic structure, optical properties, x-ray absorption spectra (XAS), and XMCD in the SCRO/BTO heterostructures. In Sec. IV, we investigate the temperature dependence of the magnetization, spin, and orbital magnetic moments, as well as the magnetocrystalline anisotropy energy in the SCRO on the BTO substrate. Our theoretical results are compared to the experimental measurements. Finally, the results are summarized in Sec. V.

II. COMPUTATIONAL DETAILS

a. Magnetocrystalline anisotropy. Magnetic anisotropy is an important parameter, since it determines the extent to which the magnetization retains its orientation in response to a magnetic field. As the most important magnetic anisotropy term, the magnetocrystalline anisotropy is related to the crystal symmetry of a material. The magnetocrystalline anisotropy energy describes the tendency of the magnetization to align along specific spatial directions rather than to randomly fluctuate over time. Whereas the exchange interaction among electron spins is purely isotropic, the orbital magnetization, via the spin-orbit interaction, connects the spin magnetization to the atomic structure of a magnetic material, hence giving rise to magnetic anisotropy [27]. It should be noted that for systems with strong structural anisotropy one may have effective anisotropic exchange among spins in a lattice mediated by the anisotropic interaction among localized and delocalized orbitals.

The calculation of the magnetocrystalline anisotropy energy has been a long-standing problem. At the early stage it was treated in a perturbative way [28,29]. Recent investigations elaborated the MAE problem using *ab initio* calculated energy

bands obtained within the local-spin density approximation (LSDA) [30–32]. The calculation of the MAE from first principles poses a great computational challenge. The prime obstacle is the smallness of the MAE, which is of only a few meV/atom, a value that must be obtained from the difference of two total energies for different magnetization directions, which are both of the order of 4×10^4 eV/atom. Owing to this numerical problem, it remained at first unclear if the LSDA could at all describe the MAE correctly, since a wrong easy axis was obtained for hcp Co and fcc Ni [33]. Recent contributions aimed at improving the numerical techniques [30,31,34], and the correct easy axis was obtained for hcp Co, [30] bcc Fe, and fcc Co [31] as well as for some other complex compounds [35–37].

For the materials exhibiting uniaxial anisotropy, such as a tetragonal crystal, the MAE can be expressed as [38]

$$\Delta E(\theta, \phi) = K_1 \sin^2\theta + K_2 \sin^4\theta + K_3 \sin^4\theta \sin 2\phi, \quad (1)$$

where K_i is the anisotropy constant of the $2i$th order, θ and ϕ are the magnetization polar and azimuthal angles of the Cartesian coordinate system where the c axis coincides with the z axis.

For orthorhombic crystals, MAE has the form [39,40]

$$\Delta E(\theta, \phi) = K_1 \sin^2\theta + K_2' \sin^2\theta \cos 2\phi + K_2 \sin^4\theta + K_3 \sin^4\theta \sin 2\phi. \quad (2)$$

The MAE for a rhombohedral crystal is [38]

$$\Delta E(\theta, \phi) = K_1 \sin^2\theta + K_2' \sin^2\theta \cos 2\phi + K_2 \sin^4\theta + K_3' \cos\theta \sin^3\theta \cos 3\phi. \quad (3)$$

Both the dipolar interaction and the spin-orbit coupling give rise to the MAE, the former contributing only to the first-order constant K_1. Here, we deal with the MAE caused only by the spin-orbit interaction. Both magneto-optical effects and the MAE have a common origin in the spin-orbit coupling and exchange splitting. Thus a close connection between the two phenomena seems plausible. In this paper, the MAE is defined as the difference between two self-consistently calculated fully relativistic total energies for two different crystallographic directions, $\Delta E(\theta, \phi) = E(\theta, \phi) - E_{\langle 001 \rangle}$.

b. Structural models. Barium titanate is the prototype ferroelectric. Its crystallographic structure shows a variety of phase transitions, dependent on the temperature [26,41]. Above 393 K, bulk BTO is cubic [$Pm\bar{3}m$; group number 221, see Fig. 1(b)] and paraelectric. Below 393 K, it becomes ferroelectric and its lattice structure changes to tetragonal ($P4/mmm$). Within the ferroelectric state, the lattice symmetry is further reduced to orthorhombic (below 278 K), and finally to rhombohedral (below 183 K). The dielectric constant, the spontaneous polarization, as well as the lattice constants change abruptly at these phase transition temperatures, accompanied by a thermal hysteresis [42].

At room temperature, the crystal structure of SCRO is tetragonal ($I4/m$; group number 87) [21] [see Fig. 1(a)]. The oxygen atoms surrounding the Cr and Re sites provide the octahedral environment. SCRO/BTO heterostructure possesses tetragonal crystal structure ($P4mm$; group number 99).

Figure 1 shows three types of heterostructures used in our calculations: SCRO/BTO monolayered $(1 \times 1 \times 1)$ heterostructure, $(2 \times 2 \times 1)$ supercell heterostructure, and $(1 \times 1 \times 2)$ supercell heterostructure together with SCRO and BTO crystal structures.

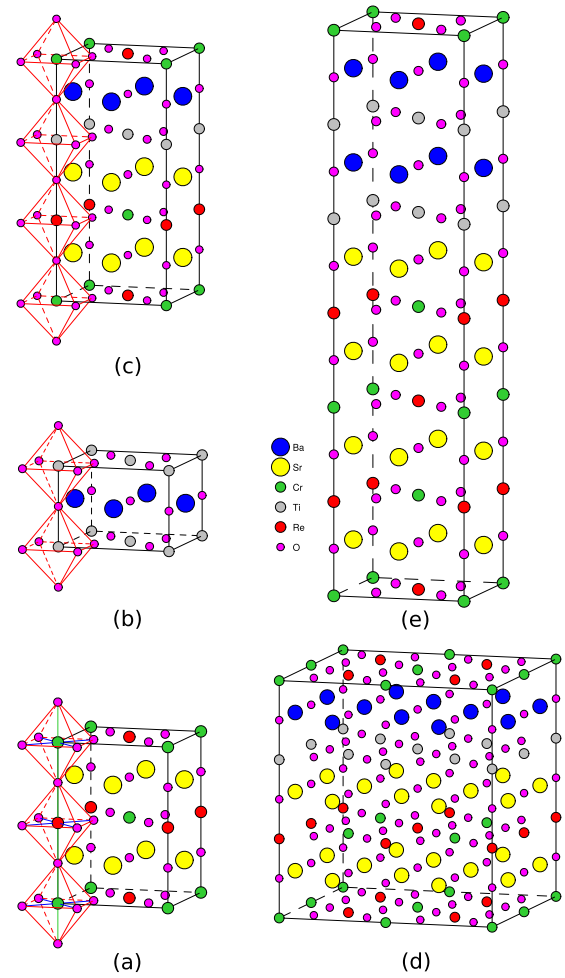

FIG. 1. Schematic representation of (a) $I4/m$ SCRO structure, (b) $Pm\bar{3}m$ BTO structure, (c) $P4mm$ SCRO/BTO monolayered $(1 \times 1 \times 1)$ heterostructure, (d) $P4mm$ SCRO/BTO $(2 \times 2 \times 1)$ heterostructure, and (e) $P4mm$ SCRO/(BTO $(1 \times 1 \times 2)$ heterostructure.

c. Calculation details. The details of the computational method are described in our previous papers [43–47], and here we only mention some aspects specific to the present calculations. The calculations presented in this work were performed using the spin-polarized fully relativistic linear-muffin-tin-orbital (LMTO) method [48,49] for the experimentally measured lattice parameters [26]. Our implementation of the LMTO method uses four-component basis functions constructed by solving the Dirac equation inside an atomic sphere [50]. The LSDA part of the calculations was based on the spin-density functional with the Perdew-Wang [51] of the exchange-correlation potential. The exchange-correlation functional of a GGA-type was also used in the version of Perdew, Burke, and Ernzerhof [52]. The basis consisted of the s, p, and d LMTO's for O sites and empty spheres, the s, p, d, and f LMTO's for Ti, Cr, Sr, and Re sites, and the s, p, d, f, and g LMTO's for Ba sites. The **k**-space integrations were performed with the improved tetrahedron method [53]. To attain good convergence in total energy, a large number

of **k** points has to be used in the calculations. To resolve the difference in total energies and to investigate the convergence, we used $16 \times 16 \times 16$ BZ division. This corresponds to 4096 **k** points in the irreducible part of BZ in SCRO on BTO. The crystal structure and atomic positions at the interface of the heterostructures was optimized using the Vienna *ab initio* simulation package (VASP) [54,55].

In the x-ray absorption process, an electron is promoted from a core level to an unoccupied state, leaving a core hole. As a result, the electronic structure at this state differs from that of the ground state. In order to reproduce the experimental spectrum, self-consistent calculations should be carried out including a core hole. In this study, the core-hole effect was fully taken into account in the self-consistent iterations by removing an electron at the core orbital using the supercell approximation. The core state of the target atom in the ground state provides the initial state $|i\rangle$ for the spectral calculation. The final states $|f\rangle$ are the conduction band states obtained separately by calculations in which one of the core electrons of the target atom is placed at the lowest conduction band. The interaction and the screening of the electron-hole pair are fully accounted for by the self-consistent iterations of the final state Kohn-Sham equations. This procedure simulates the experimental situation, in which the sample can easily supply an electron to screen a localized charge produced by the core hole. Such an approach allows for the symmetry breaking of the system in a natural way, and self-consistently describes the charge redistribution induced by the core hole. A similar approximation has been used by several authors [56–61]. We should mention that the size of the supercell is important, and ultimately it should be large enough to inhibit interaction between excited atoms in neighboring supercells. In our calculations we used a $SCRO/BTO_{2\times2\times2}$ supercell. At one of the Ti (or Re) atoms we create a hole at the $2p_{1/2}$ or $2p_{3/2}$ levels separately for the self-consistent GGA calculations of the L_2 and L_3 spectra, respectively.

III. SCRO/BTO HETEROSTRUCTURES

Generally, in $3d$ transition metal oxides (TMOs), the SO coupling is typically less than 0.05 eV. This is much smaller than the other important energies in $3d$ TMOs, such as on-site Coulomb interaction energy, U (3–5 eV), and the crystal-field splitting energy, Δ (2–3 eV). Therefore the SO coupling is not dominant in determining the physical properties of $3d$ TMOs. On the other hand, in the $5d$ TMOs, the SO coupling is approximately 0.3–0.5 eV [62], and therefore should be taken into account when describing the electronic structure of $5d$ TMOs [63].

A. Electronic structure

We start with a review of the basic electronic and magnetic properties of the compounds using the standard LSDA and GGA approximations. Figure 2 presents the energy band structures of SCRO double perovskite, SCRO/BTO, and $[SCRO/BTO]_{1\times1\times2}$ heterostructures calculated in the GGA approach (the LSDA approach produces similar results). The GGA approach produces the half-metallic states in all the structures under consideration where the only contribution

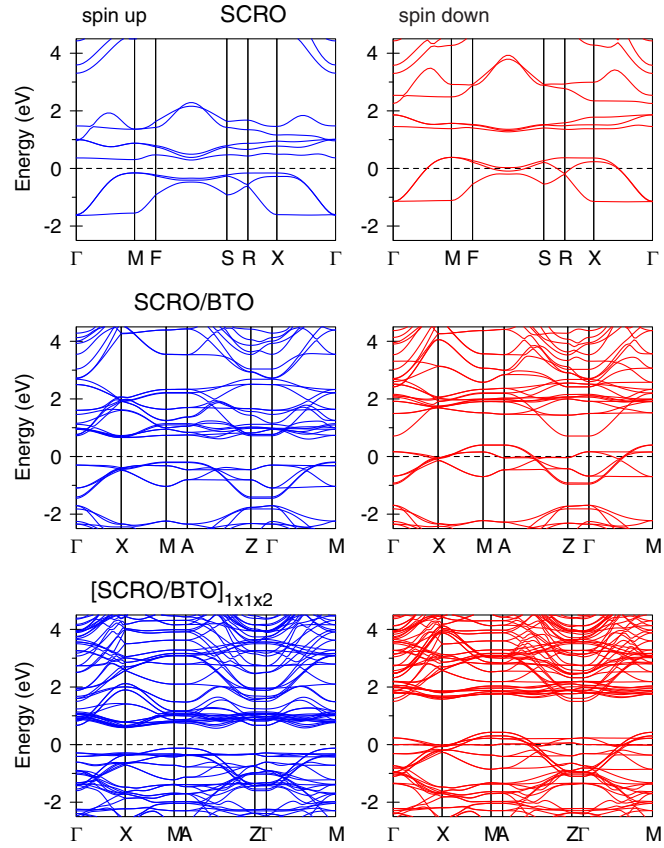

FIG. 2. The energy band structure of SCRO double perovskite, SCRO/BTO and SCRO/BTO ($1 \times 1 \times 2$) heterostructures calculated in the GGA approximation.

around the Fermi level comes from the minority spins. There is an energy gap of 0.45, 0.80, 0.70, and 0.78 eV between the Cr e_g and Re t_{2g} states in the spin-up channel for SCRO, SCRO/BTO, $[SCRO/BTO]_{1\times1\times2}$, and $[SCRO/BTO]_{2\times2\times1}$ heterostructures, respectively. A total spin magnetic moment is equal to 1 μ_B, 2 μ_B, 4 μ_B, and 8 μ_B in spin-polarized calculation (without taking into account the SO coupling) for SCRO, SCRO/BTO, $[SCRO/BTO]_{1\times1\times2}$, and $[SCRO/BTO]_{2\times2\times1}$ heterostructures, which is consistent with the expected half-metallic nature of these compounds.

The spin-resolved DOSs are presented in Fig. 3 for the SCRO/BTO heterostructure with spin-orbit coupling taking into account (GGA+SO approximation). The crystal field at the transition metal site (C_{2V} point symmetry) causes the splitting of d orbitals into a five singlets a_1, a_1, b_1, a_2, and b_2 ($3z^2-1, x^2-y^2, xz, xy$, and yz, respectively). The electronic energy bands between -19.6 and -15.5 eV are dominated by O $2s$ states. O $2p$ states are occupied the -7.5 to -1.8 eV energy interval. Spin-orbit doublet of quasi-core Ba $5p_{1/2}$ and $5p_{3/2}$ states are situated inside of the valence band at the -10.7 and -13.3 eV energy interval. There is a small amount of Ba $5d$ hybridized valence states at -2 to -6.5 eV. Ba $5d$ empty states are situated at the 3.5 to 8.5 eV above the Fermi level with narrow Ba $4f$ empty states just above them at the 8 to 9.6 eV. Occupied Cr $3d$ spin-up states at -0.2 to -1.4 eV are a combination of the x^2-y^2 and yz orbitals, the same orbitals create a narrow spin-down empty state at the 1.5 to

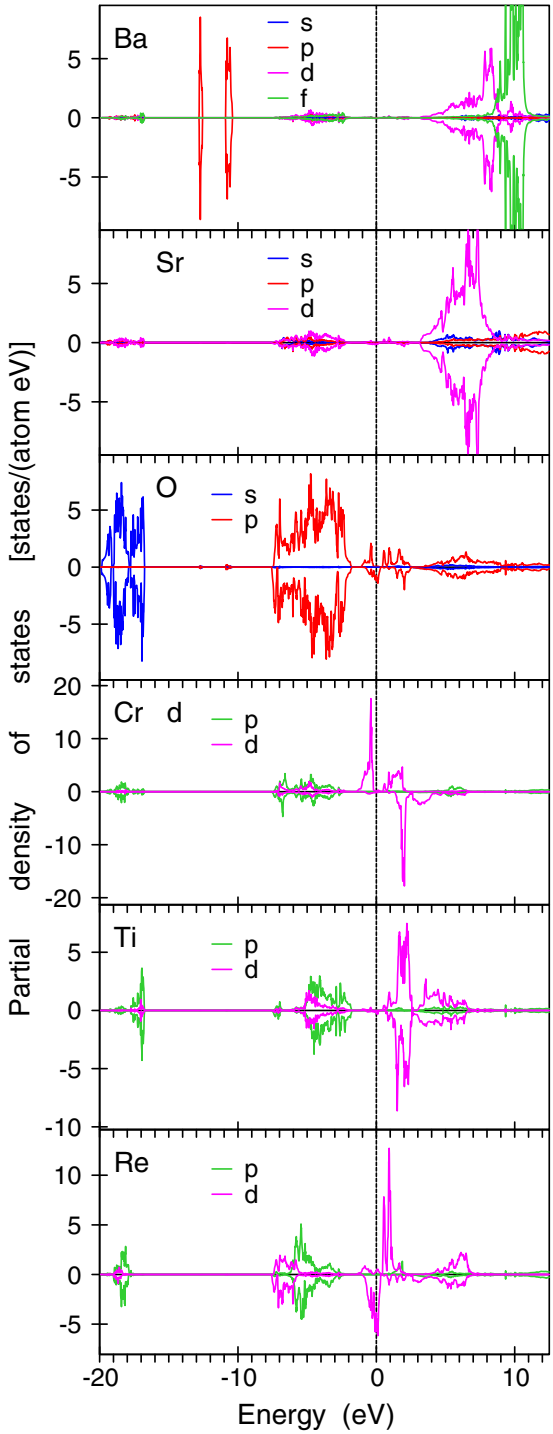

FIG. 3. The partial DOSs [in states/(atom eV)] of SCRO/BTO calculated in the GGA+SO spin-polarized approximation. The p partial DOSs at the Cr, Ti, and, Re are multiplied by the factor of 10.

2.2 eV above the Fermi level. Spin-up states above the Fermi level at the 1 to 2 eV consist of the $3z^2 - 1$ and xy orbitals. The energy states in close vicinity of the Fermi level at the Re site are also derived from purely the $x^2 - y^2$ and yz orbitals. However, due to smaller exchange splitting and the opposite spin magnetic moment direction (see Table I) the Re $5d$ empty spin-up states are situated closer to the Fermi level at the 0.6 to 1.2 eV. Besides, Fermi level crosses spin-down Re $5d$ states of the $x^2 - y^2$ and yz orbitals, they are situated at the -0.8 to 0.4 eV (Fig. 3).

TABLE I. The theoretically calculated and the experimentally measured spin, M_s, and orbital, M_l, magnetic moments (in μ_B) at the Cr, Re, Ti, Sr, Ba, and O sites of SCRO double perovskite and SCRO/BTO$_{1\times1\times1}$ heterostructure.

		SCRO		SCRO/BTO	
Atom	Method	M_s	M_l	M_s	M_l
Cr	GGA+SO	2.239	−0.038	2.543	−0.053
	Theory [69]	2.17	−0.03		
	Theory [70]	2.52	−0.04		
Re	GGA+SO	−1.087	0.286	−1.157	0.379
	Sum rules	−0.740	0.236		
	Exp. [71] (XMCD)	−0.68	0.25		
	Theory [72]	−0.78	0.20		
	Theory [70]	−1.31	0.69		
Ti	GGA+SO	–	–	−0.009	0.010
Sr	GGA+SO	−0.012	0.001	−0.010	0.001
Ba	GGA+SO	–	–	−0.002	0.002
O	GGA+SO	−0.021	0.004	−0.024	0.004

The occupation number of Ti $3d$ is equal to 1.87 electrons. Most Ti $3d$ states are empty. They are subdivided into two groups. The states occupying the energy interval between 0.6 to 2.7 eV have $x^2 - y^2$ and yz character. The high energy states at the 3.1 to 6.8 eV consist of the $3z^2 - 1$ and xy orbitals.

The Fermi energy falls in an energy gap of about 0.8 eV in the majority spin channel, between the fully filled Cr t_{2g} and empty Re t_{2g} bands. Thus the GGA calculation produces in SCRO/BTO a half-metallic ferrimagnet.

B. Magnetic moments

In magnets, the spin, M_s, and orbital, M_l, magnetic moments are basic quantities and their separate determination is therefore important. Methods of their experimental determination include traditional gyromagnetic ratio measurements [64], magnetic form factor measurements using neutron scattering [65], and magnetic x-ray scattering [66]. In addition to these, the x-ray magnetic circular dichroism combined with several sum rules [67,68] has attracted much attention as a method of site- and symmetry-selective determination of M_s and M_l. Table I presents the comparison between calculated and experimental magnetic moments at the Cr, Re, Ti, Ba, Sr, and O sites of SCRO double perovskite and SCRO/BTO$_{1\times1\times1}$ heterostructure.

The Cr and Re spin and orbital moments are antiparallel in the SCRO double perovskite and SCRO/BTO$_{1\times1\times1}$ heterostructure, in accordance with Hund's third rule. The GGA+SO Cr spin moment of 2.239 μ_B as well as the orbital moment -0.038 μ_B are in good agreement with the previous calculations [69,70] in SCRO. Our Re spin magnetic moment in SCRO is slightly larger than the results of Refs. [70,72], as well as the experimental data [71], but still larger than the data of Wang *et al.* [70]. The results from different calculations

may vary somewhat since the calculated moments depend on the details of the calculations and especially on the sizes of the muffin-tin spheres which usually differ from each other for different calculations.

Majewski *et al.* [71] have extracted the spin and orbital magnetic moments, M_s and M_l, of Re using the experimentally measured XAS and XMCD spectra at the Re $L_{2,3}$ edges, they used $n_h = 5.3$ for the number of $5d$ holes. They obtained $M_s = -0.68\ \mu_B$ and $M_l = 0.25\ \mu_B$. Both the spin and otbital moments are smaller than the ones from our first-principles calculations (Table I). Because of the significant implications of the sum rules, numerous experimental and theoretical studies aimed at investigating their validity for itinerant magnetic systems have been reported, but with widely different conclusions. The claimed adequacy of the sum rules varies from very good (within 5% agreement) to very poor (up to 50% discrepancy) [73,74]. This lack of a consensus may have several origins. XMCD sum rules are derived within an ionic model using a number of approximations. For $L_{2,3}$, they are [73] the following: (1) ignoring the exchange splitting of the core levels; (2) replacing the interaction operator $\alpha \cdot \mathbf{a}_\lambda$ by $\nabla \cdot \mathbf{a}_\lambda$; (3) ignoring the asphericity of the core states; (4) ignoring the difference of $d_{3/2}$ and $d_{5/2}$ radial wave functions; (5) ignoring $p \rightarrow s$ transitions; and (6) ignoring the energy dependence of the radial matrix elements. On the experimental side, the indirect x-ray absorption techniques, i.e., the total electron and fluorescence yield methods, are known to suffer from saturation and self-absorption effects that are very difficult to correct for [75]. The total electron yield method can be sensitive to the varying applied magnetic field, changing the electron detecting efficiency, or, equivalently, the sample photocurrent. The fluorescence yield method is insensitive to the applied field, but the yield is intrinsically not proportional to the absorption cross section, because the radiative to nonradiative relative core-hole decay probability depends strongly on the symmetry and spin polarization of the XAS final states [76]. Besides, the experimentally measured Re $L_{2,3}$ x-ray absorption spectra have a large background scattering intensity [see Fig. (7) below] and the integration of the corresponding XASs may lead to an additional error in the estimation of the magnetic moments using the sum rules.

It is interesting to compare the spin and orbital moments obtained from the theoretically calculated XAS and XMCD spectra through sum rules with directly calculated values in order to avoid additional experimental problems. The number of Re $5d$ electrons is calculated by integrating the occupied d partial density of states inside the corresponding atomic sphere, which gives the value $n_h = 5.425$. Sum rules give the spin and orbital magnetic moments equal to $M_s = -0.740\ \mu_B$ and $M_l = 0.236\ \mu_B$. These values are closer to the experimentally estimated ones from sum rules [71].

Spin and orbital magnetic moments are increased in absolute value going from SCRO to SCRO/BTO heterostructure both at the Cr and Re sites (Table I). The spin magnetic moments change to $2.557\ \mu_B$ and $2.464\ \mu_B$ at the Cr site and to $-1.177\ \mu_B$ and $-1.092\ \mu_B$ at the Re site in $[SCRO/BTO]_{1\times1\times2}$ and $[SCRO/BTO]_{2\times2\times1}$ heterostructures, respectively. We can conclude that both the spin and orbital magnetic moments are changed only slightly in different heterostructures.

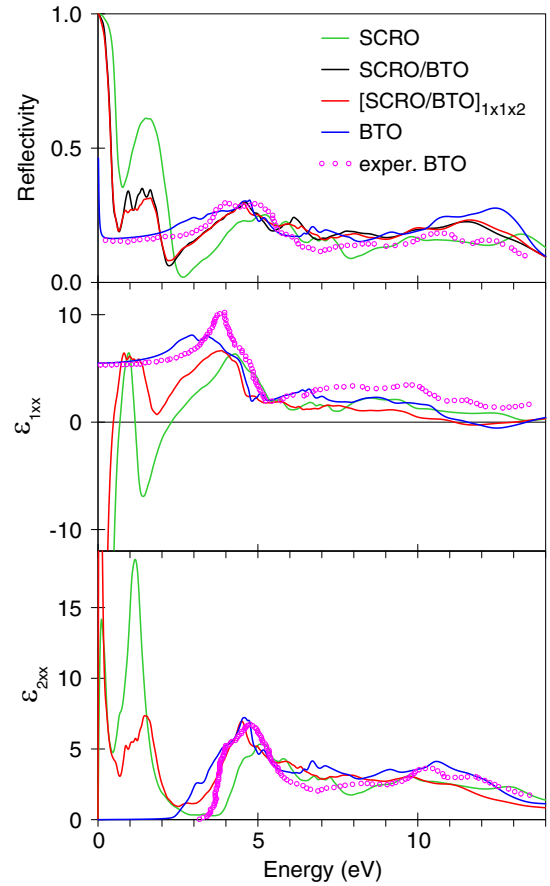

FIG. 4. The experimentally measured [77] diagonal optical reflectivity spectra (top) and dielectric functions ε_{1xx} (middle) and ε_{2xx} (bottom) of BTO (open magenta circles), and the spectra calculated by the SPR LMTO method in the GGA+SO approximation for BTO (blue curves), SCRO double perovskite (green curves), SCRO/BTO monolayered ($1 \times 1 \times 1$) heterostructure (black curve), and ($1 \times 1 \times 2$) supercell heterostructure (red curves).

The hybridization between Ti and other transition metal d states plays an important role in the formation of the band structure of SCRO/BTO heterostructures. It leads to the induced spin and orbital magnetic moments at the Ti sites. The Sr, Ba, and O sites also possess small induced spin and orbital magnetic moments (see Table I).

C. Optical properties

Among the various properties of crystalline solids, the optical response to incident light is one of the standard phenomena used to characterize materials. Figure 4 shows the experimentally measured [77] diagonal optical reflectivity spectra (top) and dielectric functions ε_{1xx} (middle) and ε_{2xx} (bottom) of BTO (open magenta circles), and the spectra calculated by the SPR LMTO method in the GGA+SO approximation for BTO (blue curves), SCRO double perovskite (green curves), SCRO/BTO monolayered ($1 \times 1 \times 1$) heterostructure (black curves), and ($1 \times 1 \times 2$) supercell heterostructure (red curves). In the following, ε_{1xx} and ε_{2xy} denote the dispersive and absorptive parts, respectively, of the complex diagonal dielectric function $\varepsilon_{xx} = \varepsilon_{1xx} + i\varepsilon_{2xx}$.

Optical interband transitions in BTO take place between nine valence bands derived from O $2p$ orbitals separated by a direct gap of 2.35 eV at the Γ point to the Ti $3d$-derived conduction bands (not shown). The energy gap is somewhat lower than the experimental band gap of 3.2 eV for BTO [78]. The origin of this discrepancy may be the GGA approximation, which underestimates the band gaps even for insulators. Our theoretical calculations are in good agreement with previous calculations [77,79,80] and describe well the shape and energy positions of the major peaks in the optical reflectivity spectrum as well as in the dielectric function $\varepsilon(\omega)$. However, due to underestimation of the energy gap, the optical absorption starts at smaller energies in our calculations in comparison with the experimental data (see bottom of Fig. 4). It also affects the low energy part of the $\varepsilon_{1xx}(\omega)$ function at 3 to 4 eV (middle panel of Fig. 4).

The optical reflectivity spectrum of SCRO double perovskite has two deep local minima at 0.8 and 2.8 eV. The absorptive part of the dielectric function, $\varepsilon_{2xx}(\omega)$, shows a strong peak at around 1 eV. Our theoretical calculations of the optical properties of SCRO are in good agreement with previous calculations by Das *et al.* [69].

Figure 4 also presents the optical spectra for the SCRO/BTO monolayered $(1 \times 1 \times 1)$ heterostructure (black curve) and $(1 \times 1 \times 2)$ supercell heterostructure (red curves). We found that the optical spectra for different types of supercell heterostructures are pretty much the same. The optical spectra for the $(1 \times 1 \times 2)$ supercell heterostructure are slightly more smooth functions of energy in comparison with the SCRO/BTO monolayered $(1 \times 1 \times 1)$ heterostructure (compare red and black curves on top of Fig. 4). The optical reflectivity spectrum for the SCRO/BTO heterostructure has deeper minimum at the 0.8 eV in comparison with the SCRO spectrum. The strong peak appearing at 1 eV in the $\varepsilon_{2xx}(\omega)$ dielectric function of SCRO perovskite is significantly reduced in the SCRO/BTO heterostructure (bottom of Fig. 4).

D. XMCD spectra

The XMCD is a powerful tool to study the element-specific local magnetic interactions and also it reflects the spin and orbital polarizations of the local electronic states. The XMCD experiments measure the difference of the absorption of x rays with opposite (left and right) directions of circular polarization. Let us first consider the XAS and XMCD properties of the ions that became magnetic in the SCRO/BTO heterostructure, namely, Ti and Ba.

The XAS spectra of the ferroelectric barium titanate BTO at the Ti $L_{2,3}$ edges have been investigated experimentally, as well as theoretically by several authors [81–83]. Figure 5 (top) presents the experimental x-ray absorption spectrum [81] (open circles) at the Ti $L_{2,3}$ edges in BTO compared with the calculated ones for BTO (dashed red curve) and SCRO/BTO heterostructure (full blue curve). The bottom of Fig. 5 shows the calculated XMCD spectrum at the Ti $L_{2,3}$ edges in the SCRO/BTO heterostructure. The experimentally measured Ti $L_{2,3}$ XAS consists of four major peaks in the range of 455–466 eV. The two peaks with lower energy are the Ti-L_3 edge, while the two peaks with higher energy are the Ti-L_2 edges. It is well known that when the Ti ion is octahedrally

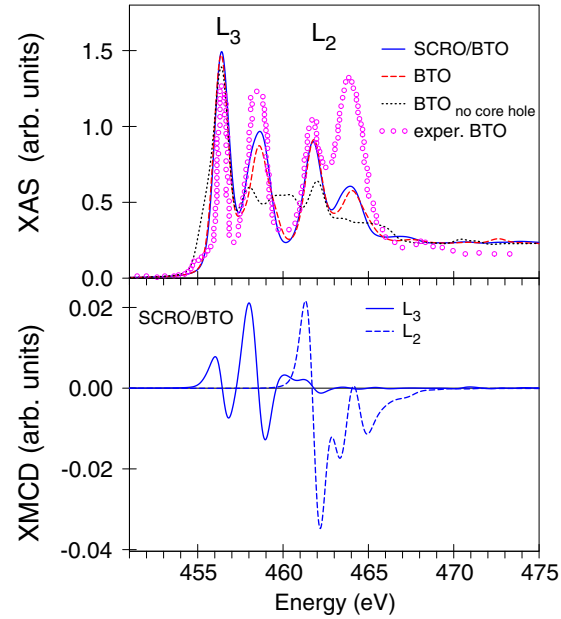

FIG. 5. (Top) The experimental x-ray absorption spectrum [81] (open circles) at the Ti $L_{2,3}$ edges in BTO compared with the theoretically calculated ones for BTO with the core-hole effect taken into account (dashed red curve), BTO without the core-hole effect taken into account (dotted black curve), and SCRO/BTO heterostructure (full blue curve). (Bottom) Theoretically calculated XMCD spectrum at the Ti $L_{2,3}$ edges in SCRO/BTO heterostructure.

coordinated, the two peaks of Ti L_3 and L_2 will split into two main separate peaks e_g and t_{2g} [84]. The separation between these two main peaks is associated with the crystal-field splitting modified by the exchange interaction. Because the SO splitting of the core Ti $2p$ level ($\Delta E_{\mathrm{SO}} = 5.74\,\mathrm{eV}$) and the Ti $3d$ crystal-field splitting modified by the exchange interaction ($\Delta E_{\mathrm{CF}} = 3.3\,\mathrm{eV}$) are of the same order of magnitude, the L_3 and L_2 x-ray absorption spectra are strongly overlapped. The four experimentally observed intense peaks from 455 to 466 eV can be, to a first approximation, assigned to $2p_{3/2} \rightarrow e_g$, $2p_{3/2} \rightarrow t_{2g}$, $2p_{1/2} \rightarrow e_g$, and $2p_{1/2} \rightarrow t_{2g}$ transitions, respectively. However, the $2p_{1/2} \rightarrow e_g$ and $2p_{1/2} \rightarrow t_{2g}$ transitions (L_2 spectrum) contribute also to the two low energy peaks.

As expected from the Ti^{4+} ions and their octahedral coordination, BTO and SCRO/BTO heterostructure have similar spectra, as shown in Fig. 5. This demonstrates that there is no difference in the chemical environments of Ti ions. For the whole multilayered films, Ti^{4+} is in octahedral coordination with oxygen, with all octahedra sharing corners. The theory reproduces the energy position of all the fine structures quite well, however, does not reproduce the experimentally observed L_3/L_2 x-ray absorption ratio. It is well known that the L_2 and L_3 absorption channels in early $3d$ transition metals with nearly empty d bands are strongly coupled through the photoelectron-core-hole Coulomb and exchange interactions [85–88]. This leads to a branching ratio close to 1:1, far from the statistical ratio 2:1, which is obtained in the single-particle theory, unless the SO interaction in the final $3d$ band is considered. From our band structure calculations, we obtained an L_3/L_2 branching ratio equal to 1.65, which is far from the

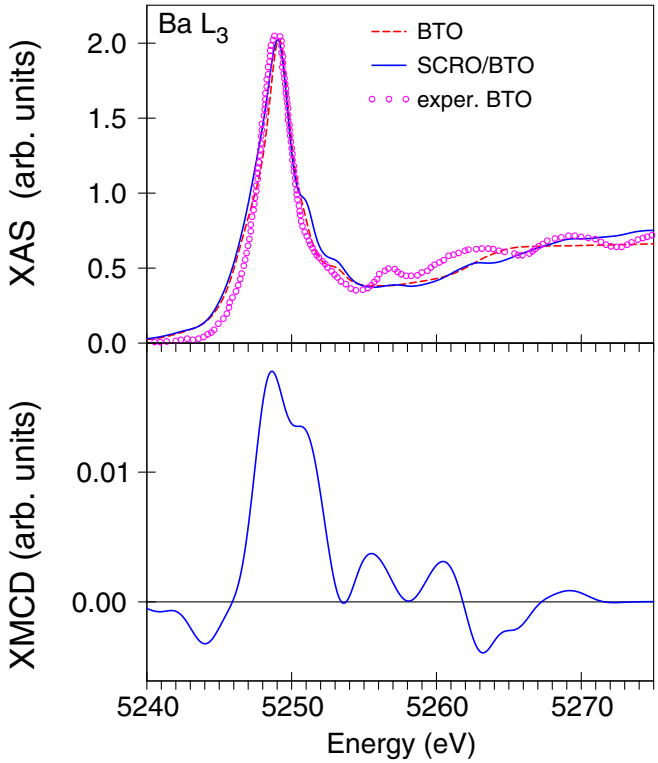

FIG. 6. (Top) The experimental x-ray absorption spectrum [89] (open circles) at the Ba L_3 edge in BTO compared with the theoretically calculated ones for BTO (dashed red curve) and SCRO/BTO heterostructure (full blue curve). (Bottom) Theoretically calculated XMCD spectrum in SCRO/BTO heterostructure at the Ba L_3 edge.

experimentally observed. This problem can be accounted for through many-electron calculations and we will address it in future investigations.

We investigate also the core-hole effect in the final state using the supercell approximation where the excited atom is formally treated as an impurity. We found that the core-hole interactions significantly improve the agreement between the calculated and measured Ti $L_{2,3}$ XAS spectra in BTO [Fig. 5 (top)].

Pure BTO possesses no dichroism because all ions in BTO are nonmagnetic. However, due to the hybridization between Ti d states and Cr/Re d states in SCRO/BTO heterostructures, there are induced spin and orbital magnetic moments at the Ti sites (see Table I). Therefore one would expect a well pronounced XMCD signal at the Ti $L_{2,3}$ edges (bottom of Fig. 5). The experimental measurements of the XMCD spectra at Ti $L_{2,3}$ edges in SCRO/BTO are highly desirable.

The XAS spectra of the ferroelectric barium titanate BTO at the Ba L_3 edge have been investigated experimentally, as well as theoretically by several authors [89,91–95]. Figure 6 shows the experimental x-ray absorption spectrum [89] (open circles) at the Ba L_3 edge in BTO compared with the theoretically calculated ones for BTO (dashed red curve) and SCRO/BTO heterostructure (full blue curve). The bottom of Fig. 6 presents the theoretically calculated XMCD spectrum in the SCRO/BTO heterostructure at the Ba L_3 edge.

On the basis of the dipole selection rule, the large white line in BTO at around 5249 eV is ascribed to the resonant excitation from Ba $2p_{3/2}$ to the Ba $5s$ and $5d$ unoccupied states. The low- and high-energy regions could be tentatively attributed to the hybridization of Ba $5d$ with O $2p$ orbitals. The spectrum was calculated with taking into account of a Ba $2p_{3/2}$ core hole and convoluted by a 1-eV Lorentzian contribution accounting for the core-hole lifetime broadening. We found that the core-hole effect has a small influence on the shape of the Ba L_3 XAS spectrum. The theoretically calculated spectrum well reproduces the overall profile, including the low- and high-energy regions noted above and the small peaks at the high energies above the white line. Yoshii *et al.* [95] show that the Ba L_3 XAS spectra show no apparent change between the room-temperature paraelectric cubic phase and ferroelectric tetragonal phase at 150 °C. On the basis of the discussion in Ref. [96], the absence of temperature dependence of the spectrum implies the absence of atomic displacement around Ba^{2+} ion. The Ba L_3 XAS spectra also have almost the same shape in pure BTO and in SCRO/BTO heterostructure. The high-energy shoulders at around 5251.5 and 5253.5 eV are better pronounced in the heterostructure.

Figure 7 shows the calculated XAS (top) and XMCD (bottom) spectra at the Re $L_{2,3}$ edges in the SCRO double perovskite (full blue curve) and SCRO/BTO heterostructure (dashed green curve), together with the experimental spectra for the SCRO [90] (open circles). The theoretically calculated Re L_2 and L_3 XAS spectra for these structures have a high resemblance to each other with the double peak structure. The energy splitting of these peaks is generally ascribed to the crystal field splitting of d orbitals into t_{2g} and e_g states [97].

The XAS and XMCD spectra at the Re $L_{2,3}$ edges are very similar for SCRO double perovskite and SCRO/BTO heterostructures. We can conclude that the presence of the BTO layer in SCRO/BTO heterostructures only moderately changes the magnetic structure of the SCRO layer. A similar situation was found also for the Cr $L_{2,3}$ XAS and XMCD spectra. They are very similar for pure SCRO and SCRO/BTO multilayers (not shown). It is interesting to note that the GGA+SO+U approximation with the screened Coulomb $U_{\mathrm{Re}} = 2$ eV and exchange Hund coupling $J_{\mathrm{Re}} = 0.7$ eV strongly overestimates the circular dichroism at the Re L_2 edge (dotted black curve in bottom of Fig. 7).

IV. SCRO ON THE BTO SUBSTRATE

Czeschka *et al.* [25] and Opel *et al.* [26] have grown ferromagnetic double perovskite SCRO as epitaxial thin film onto ferroelectric BTO. The experiments show a giant change of the magnetic anisotropy in SCRO film and huge coercive fields, depending on the substrate-induced strain state. Due to coherent growth, the in-plane lattice constants and crystal structure type of the SCRO film follow those of the BTO substrate as a function of temperature. In particular, the crystal structure of SCRO is changed from tetragonal structure above 278 K to orthorhombic one below this temperature, and a rhombohedral type below 183 K. The thickness of epitaxial SCRO thin film on BTO is rather large (810 Å [25,26]). In the following, the effect of the BTO substrate on SCRO will be taken into account only through the structural phase transitions dependence of the BTO on the temperature.

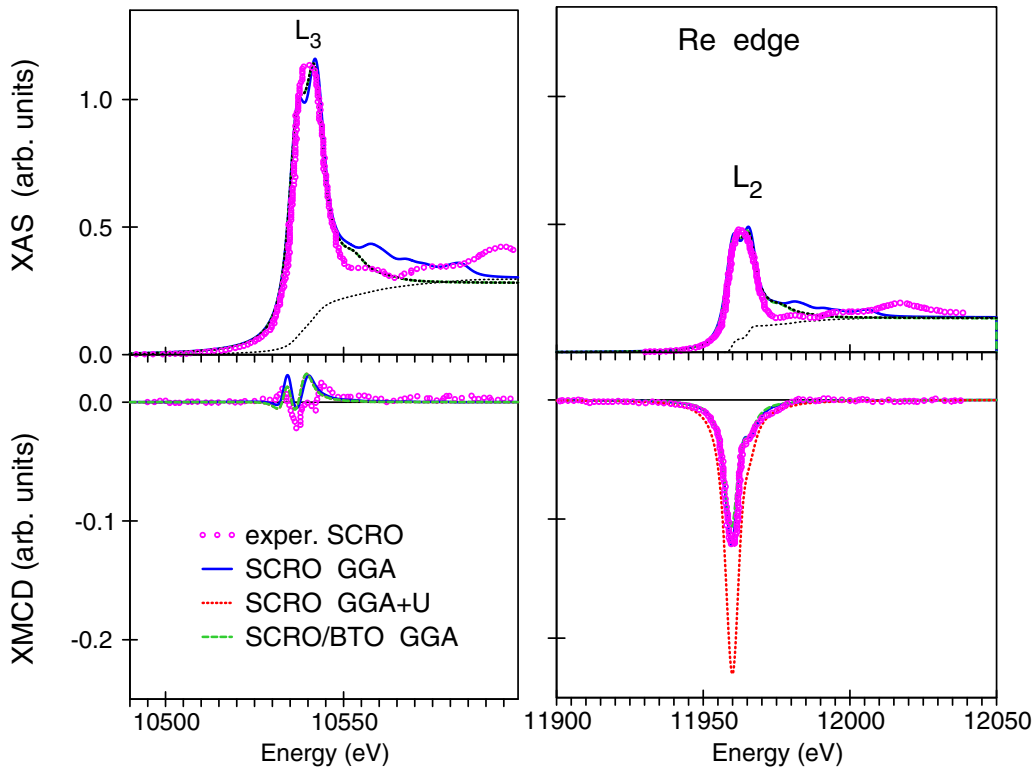

FIG. 7. (Top) The experimental x-ray absorption spectrum [90] (open circles) at the Re $L_{2,3}$ edges in SCRO compared with the calculated ones for SCRO (full blue curves) and SCRO/BTO heterostructure (dashed green curves). (Bottom) The calculated XMCD spectra at the Re $L_{2,3}$ edges for SCRO in the GGA+SO (full blue curves) and GGA+SO+U approximation (dotted red curve) with the screened Coulomb $U_{\mathrm{Re}} = 2\,\mathrm{eV}$ and exchange Hund coupling $J_{\mathrm{Re}} = 0.7\,\mathrm{eV}$; dashed green curves present the spectra for the SCRO/BTO heterostructure in the GGA+SO approximation.

A. Temperature dependence of the magnetization

Opel *et al.* [26] determined the a and c lattice parameters both for BTO substrate and SCRO thin film. The results are displayed in Figs. 8(a) and 8(b). All data were obtained with decreasing temperature. The c-axis lattice parameter of the BTO substrate [Fig. 8(a)] follows well the behavior reported for bulk BTO material [41]. It is slightly above $c = 4.01$ Å in the cubic phase, then increases to $c = 4.025, \ldots, 4.04$ Å, (tetragonal), drops to $c = 4.02$ Å (orthorhombic), and finally becomes $c = 4.005$ Å (rhombohedral). Also the a parameter behaves as expected in the tetragonal phase. For the SCRO thin film [Fig. 8(b)], the a-axis parameter shows the same temperature dependence as for the substrate. This confirms coherent growth and biaxial strain transfer from BTO into the epitaxial film. Also the c lattice parameter follows the trend of the substrate. In the tetragonal phase, however, it does not display any temperature dependence, in contrast to the behavior of BTO. In summary, the structural analysis shows that the in-plane lattice constants and crystal structure type of the SCRO film follow those of the BTO substrate as a function of temperature. In particular, the epitaxial coherency strain in the SCRO film abruptly changes at the structural phase transitions of BTO.

The magnetic properties of SCRO on BTO were determined by a SQUID magnetometer with a magnetic field of 1 T applied in the film plane [26]. At the BTO phase transitions, large steplike changes of the magnetization M have been observed, which drops at the tetragonal-orthorhombic transition and increases again when entering the rhombohedral phase. These "jumps" are as large as 5.0% (rhombohedral/orthorhombic) and 4.2% (orthorhombic/tetragonal) and therefore by a factor of 5 larger than what was expected from a pure geometric effect [25]. A careful investigation [25] shows that the values for saturation magnetization, remanent magnetization, and coercivity clearly differ from each other for the different structural phases of the substrate. Therefore the observed discontinuities are attributed to a change of the magnetic anisotropy of thin SCRO layer. They are induced by abrupt changes of the epitaxial coherency strain due to the structural phase transitions of the BTO substrate.

In the vicinity of a second-order phase transition PM-FM phase, the critical behavior of the spontaneous magnetization M near T_C is characterized by a critical exponent β. The scaling hypothesis suggests the following relation near the critical region defined by [98,99]

$$M(T) = M_0|-\varepsilon|^{\beta}, \quad \varepsilon < 0, \quad T < T_C, \tag{4}$$

where $\varepsilon = (T - T_C)/T_C$ is the reduced temperature and M_0 is the critical amplitude.

The critical exponent as well as the critical amplitude M_0 exhibit universal behavior near the phase transition. There are several universality classes with sets of critical indices that depend on the spin and the system dimensionality. For a first-order ferromagnetic phase transition, however, the critical exponent is impossible to define unambiguously because the

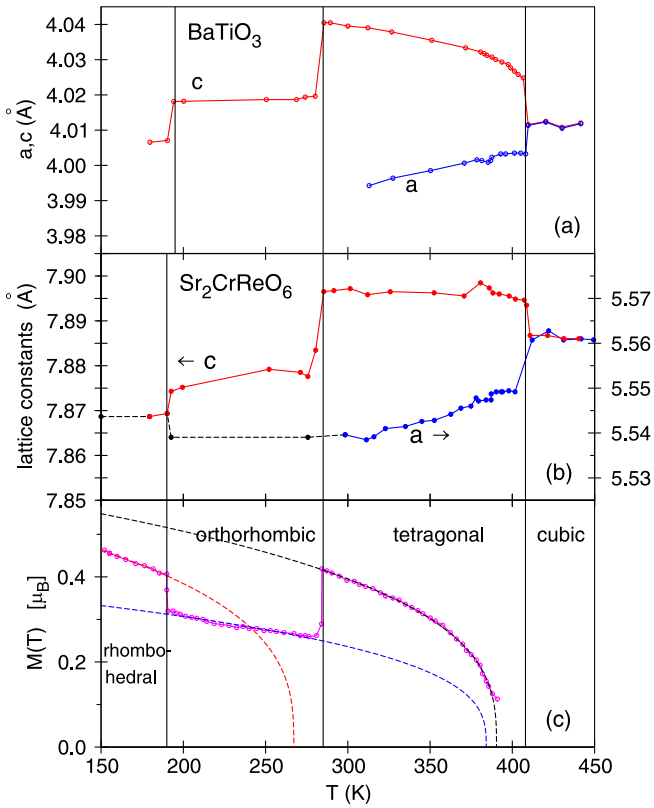

FIG. 8. (a) Lattice parameter a (blue circles) and c (red circles) of the $BaTiO_3$ substrate as a function of temperature, determined by x-ray diffraction [26]. (b) a (blue circles, right scale) and c (red circles, left scale) for a thin film of SCRO, grown on $BaTiO_3$ substrate [26] (black circles show extrapolated values of the lattice parameter a used in our calculations). (c) The temperature dependence of the magnetization $M(T)$ (in μ_B) of thin film of SCRO (magenta circles), grown on $BaTiO_3$ substrate; a magnetic field of 1 T was applied in the film plane [26].

temperature $T_C(H)$ depends on the applied magnetic field [100].

The critical exponent β varies from 0.1 to 0.5 in manganites with perovskite structure using different theoretical models: mean-field ($\beta = 0.5$), 3D-Heisenberg ($\beta = 0.365$), 3D-Ising ($\beta = 0.325$), and critical mean field ($\beta = 0.25$) [98,99]. Our fitting of the experimentally measured temperature dependence of the magnetization $M(T)$ presented in Fig. 8(c) gives the value of parameter $\beta = 0.335$ for the tetragonal phase. This value was fixed and used for the fitting $M(T)$ for the orthorhombic and rhombohedral phases. We found that the value of Curie temperature is reduced through the phase transitions with decreasing temperature and is equal to 390.4 ± 0.6, 384.1 ± 15.0, and 267.2 ± 8.5 K for the tetragonal, orthorhombic, and rhombohedral phases, respectively. These values are significantly lower than the Curie temperature for pure SCRO ($T_C = 635$ K) [22,23]. The critical amplitude M_0 was found to be equal to 0.645 ± 0.012 μ_B, 0.392 ± 0.008 μ_B, and 0.610 ± 0.011 μ_B, for the tetragonal, orthorhombic, and rhombohedral phases, respectively.

It has been established that the unique temperature dependence of the magnetization of SCRO on the BTO substrate is determined by the thermal variation of the lattice parameters a and c and structure phase transitions of the BTO substrate [25,26]. In the following section, we explain experimental observations by examining the dependence of the calculated magnetic moments, total energy, and MAE on the lattice geometry. We assume that the finite temperature can be mimicked by the lattice constants corresponding to this temperature (see Fig. 8). The epitaxial SCRO thin film grows coherently on ferroelectric BTO, therefore, we also assumed the crystal symmetries and atomic positions of SCRO in accordance with the ones in BTO for tetragonal, orthorhombic, and rhomboedral phases as determined experimentally by Kwei *et al.* [101]. The construction of the corresponding SCRO crystal structures is not a trivial task. The major difference between ordered SCRO and BTO structures are in the oxygen positions. Besides, Cr and Re ions also have to be displaced from their regular positions in SCRO to fit the positions of Ti ions in the BTO. The crystal structure of SCRO on the BTO substrate is changed from tetragonal structure above 278 K to an orthorhombic one below this temperature and a rhombohedral type below 183 K. The corresponding substrate-induced SCRO structures are presented in Fig. 9.

Figure 10 shows variation of absolute values of orbital M_l and spin magnetic moments M_s at Cr and Re sites as a function of temperature. The spin magnetic moments have similar temperature and crystal structure dependence for the Cr and Re sites [Fig. 10(a)], however, the Cr and Re spin moments (as well as orbital moments) are antiparallel in the SCRO double perovskite and SCRO/BTO heterostructure (Table I). The same is true also for the case of SCRO on BTO substrate. The spin magnetic moments change monotonically with temperature before and after the phase transitions and change abruptly at the points of the phase transitions. These "jumps" are different for different sites. The spin magnetic moment increases at the tetragonal/orthorhombic phase transition with decreasing of temperature by 0.036 μ_B at the Cr site and by 0.016 μ_B at the Re site in absolute value. At the orthorhombic/rhombohedral phase transition, the spin magnetic moment decreases by 0.050 μ_B at the Cr site and by 0.031 μ_B at the Re site in absolute value.

The orbital magnetic moments at the Cr site are smaller by one order of magnitude than at the Re site and have an opposite direction. The orbital magnetic moments also have an opposite temperature and crystal structure behavior at the Cr and Re sites [Fig. 10(b)]. At the tetragonal/orthorhombic phase transition, with decreasing temperature the orbital magnetic moment decreases by 0.045 μ_B (by 19%) at the Re site and increases by 0.008 μ_B at the Cr site in absolute value. At the orthorhombic/rhombohedral phase transition, the orbital magnetic moment decreases by 0.006 μ_B at the Cr site and by 0.003 μ_B at the Re site in absolute value.

The total magnetic moment M_{total} presented in Fig. 10(c) also possesses jumps at the structural phase transitions. At the tetragonal/orthorhombic phase transition, M_{total} decreases by 0.020 μ_B with decreasing temperature and increases by 0.017 μ_B at the orthorhombic/rhombohedral phase transition. The magnetic discontinuity at the structural phase transition is due to the change of the symmetry type and also jump of the c lattice constant [see Fig. 8(b)]. The abrupt change in the c lattice constant leads to abrupt change of interatomic distances

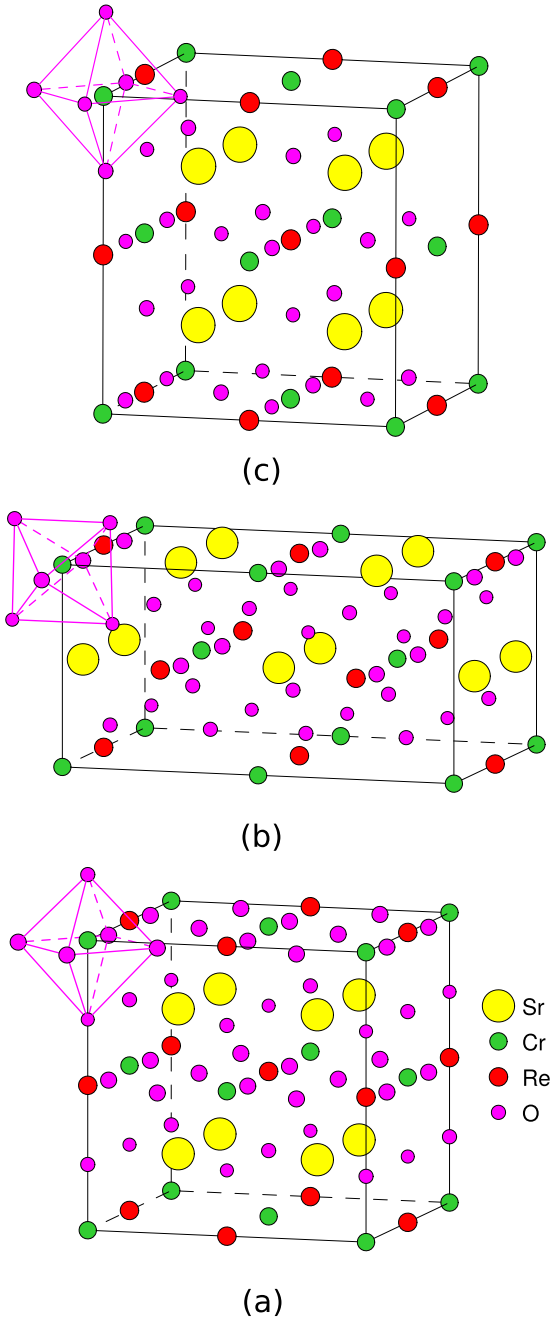

FIG. 9. Schematic representation of SCRO structures on BTO: tetragonal (a), orthorhombic (b), and rhombohedral (c) structures.

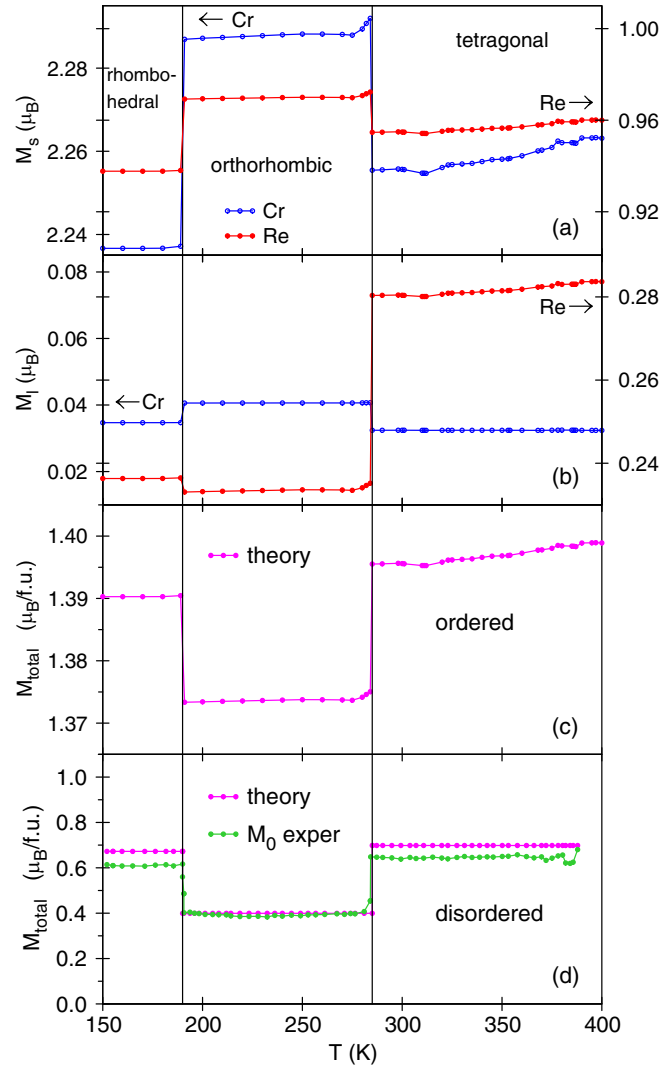

FIG. 10. Variation of absolute values of spin M_s (a) and orbital M_l (b) magnetic moments at the Cr (open blue circles) and Re (full red circles) sites in SCRO as a function of temperature in μ_B. (c) shows the temperature dependence of the total M_{total} in μ_B/f.u. in SCRO without taking into account the intersite Cr/Re disorder. The critical amplitude M_0 obtained by fitting to the measured $M(T)$ (green circles) and results of our calculations of M_{total} in μ_B/f.u. with the intersite Cr/Re disorder taken into account (magenta circles) are presented in (d). The temperature dependence of the lattice constants is taken from Ref. [26].

and interatomic *d*-*d* hybridization, as a result, a jump in the magnetic moments is appeared. However, the discontinuity of total magnetic moment is one order of magnitude smaller than the experimentally measured one. We found that the theoretically calculated temperature dependence of the total magnetic moment with 25% of the Cr/Re disorder (when one of four Cr ions are on Re site and vice versa) is in excellent agreement with the critical amplitude M_0, obtained from the fitting of the experimentally measured magnetization $M(T)$ using Eq. (4) [Fig. 10(d)]. Such effect of the Cr/Re disorder on the magnetic discontinuity at the structural phase transition is due to the magnetic reconstruction occurring in the SCRO on BTO under the disorder. The major effect comes from the reorientation of the Cr spin moments. The Cr and Re spin sublattices are ordered ferromagnetically each and ferrimagnetically to each other in all the crystal structures under consideration for ordered SCRO on BTO. The Cr/Re disorder leads to the ferrimagnetic order for both the Cr and Re sublattices. Moreover, such ferrimagnetic ordering depends on the type of the SCRO crystal structure. In the tetragonal and rhombohedral structures, one Cr ion has spin moment opposite to other Cr moments. It itself significantly reduces the total magnetic moment from 1.396 μ_B to 0.698 μ_B in the tetragonal structure and from 1.390 μ_B to 0.672 μ_B in the rhombohedral structure in agreement with the experiment

(Fig. 10). In the case of the orthorhombic crystal structure, two Cr ions have spin moments opposite to the other two Cr moments. This almost antiferromagnetic (AF) ordering of Cr ions produces a very small average spin moment at the Cr sublattice and the total magnetic moment is derived by spin and orbital magnetic moments at the Re sites. Such reconstruction produces a jump in the total magnetic moment of 0.299 μ_B at the tetragonal/orthorhombic phase transition for the Cr/Re disordered system in comparison with only 0.020 μ_B for the ordered SCRO on BTO. The orientation of the Cr spin magnetic moments plays a major role for the significant increase of magnetic discontinuity at the structural phase transition. However, one has to take into account also the spin and orbital magnetic moments at the Re sites to obtain the precise values of the total magnetic moments. In all structures, one Re ion has spin moment opposite to the other Re moments. The Re and Cr orbital magnetic moments are always antiparallel to their spin moments. It is important to note that to achieve an agreement with the experiment we have to assume AF ordering in Cr sites in the orthorhombic crystal structure. Although the ferrimagnetic order with one Cr spin moment opposite to the other three ones is slightly lower in total energy than the AF order, it produces a smaller jump in comparison with the experiment (however, still larger than in the case of ordered structure). One has to mention that the SCRO on BTO system is far from the thermodynamic equilibrium. The SCRO film is in large strain due to the pulsed laser deposition specimen preparation and relatively large mismatch between SCRO and BTO lattice constants. Therefore the total energy analysis in this case can not be valid. Another reason of the reduction of the magnetization $M(T)$ in the orthorhombic phase in comparison with the other two phases might be due to the highly twinned BTO crystal in the orthorhombic phase, which is absent for two other phases. Due to this effect, the saturation magnetization M_S in the SCRO orthorhombic phase is reduced in comparison with the tetragonal and the rhombohedral phases as can be seen from the magnetic field dependence of the magnetization $M(H)$ measured by Ceschka *et al.* [25].

B. Magnetocrystalline anisotropy

Czeschka *et al.* [25] investigated the field dependence of the magnetization in the SCRO on BTO for three different orientations of the external magnetic field: $\mathbf{H}\|\langle 100\rangle$, $\mathbf{H}\|\langle 110\rangle$, and $\mathbf{H}\|\langle 001\rangle$. The temperatures of the field sweeps were chosen slightly above and below the phase transition from tetragonal to orthorhombic 290 and 270 K and from orthorhombic to rhombohedral 200 and 180 K. They found that in the tetragonal phase of BTO, at 290 K, the hysteresis loops for the external magnetic field in-plane ($\mathbf{H}\|\langle 100\rangle$ and $\mathbf{H}\|\langle 110\rangle$) are rather wide and very similar, while for the out-of-plane direction of the magnetic field ($\mathbf{H}\|\langle 001\rangle$) the hysteresis loop is more rectangular. This might suggest that the easy magnetization axis is out-of-plane in the tetragonal phase. Similar behavior of the hysteresis loops was found also for the orthorhombic phase [25]. However, in the rhombohedral phase, all three hysteresis loops ($\mathbf{H}\|\langle 100\rangle$, $\langle 110\rangle$, and $\langle 001\rangle$) are very similar to each other. It seems that there is no preferable easy axes orientation between these three directions.

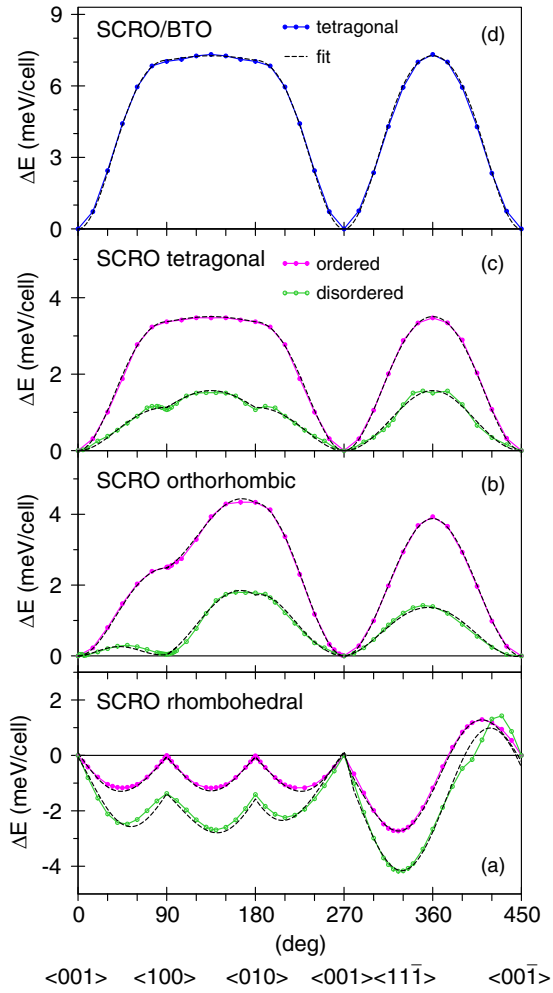

FIG. 11. The theoretical calculations of the MAE ΔE as a function of the magnetization polar θ and azimuthal ϕ angles for the rhombohedral (a), orthorhombic (b), and tetragonal (c) phases without (magenta curves) and with (green curves) taking into account the intersite Cr/Re disorder. Panel (d) shows the MAE ΔE for $[\mathrm{SCRO/BTO}]_{1\times1\times1}$ heterostructure. Black dashed curves present fitted curves of MAE using the corresponding formula 1, 2, and 3 with magnetic anisotropy constants K_i presented in Table II.

These facts are correlated with our theoretical calculations. Figure 11 shows the MAE as a function of the magnetization polar θ and azimuthal ϕ angles for the tetragonal, orthorhombic, and rhombohedral phases without (magenta curves) and with (green curves) taking into account the intersite Cr/Re disorder.

We found that the easy axis of magnetization for the tetragonal phase is along the ($\langle 001\rangle$) direction for both ordered and disordered structures. The ordered orthorhombic phase also has the easy axis of magnetization along the ($\langle 001\rangle$) direction, however, intersite Cr/Re disorder changes the easy axis of magnetization approximately to the ($\langle 00\bar{1}\rangle$) direction with $\theta = 175.6^\circ$ and $\phi = 45^\circ$ (Table II). The rhombohedral phase has the easy axis of magnetization approximately along the $\langle 11\bar{1}\rangle$ direction with $\theta = 139.8^\circ$ and $\phi = 45^\circ$ for the ordered structure and $\theta = 148.0^\circ$ and $\phi = 45^\circ$ for the disordered one. Our calculations show several local minima for the

TABLE II. Calculated easy axes, corresponding directional angles (in degree), and magnetic anisotropy constants (in meV/cell) for the SRCO, SCRO on BTO structures, and $[SCRO/BTO]_{1\times1\times1}$ heterostructure.

Structure	Type	Easy axis	θ_0	ϕ_0	K_1	K_2	K_3	K_2'	K_3'
SCRO/BTO	ordered	⟨001⟩	0	0	10.32 ± 0.08	-3.24 ± 0.10	0.19 ± 0.04	0	0
SCRO	ordered	⟨001⟩	0	0	4.50 ± 0.05	-1.12 ± 0.06	0.13 ± 0.02	0	0
Tetragonal	disordered	⟨001⟩	0	0	1.45 ± 0.07	-0.32 ± 0.07	0.44 ± 0.03	0	0
SCRO	ordered	⟨001⟩	0	0	4.11 ± 0.06	-0.70 ± 0.06	0.47 ± 0.02	-0.92 ± 0.01	0
Orthorhombic	disordered	$\approx\langle 00\bar{1}\rangle$	175.6	45	1.07 ± 0.10	-0.18 ± 0.09	0.85 ± 0.01	0.49 ± 0.02	0
SCRO	ordered	$\approx\langle 11\bar{1}\rangle$	139.8	45	-2.54 ± 0.03	~ 0	0	-1.42 ± 0.02	0.80 ± 0.04
Rhombohedral	disordered	$\approx\langle 11\bar{1}\rangle$	148.0	45	-3.44 ± 0.13	~ 0	0	-1.72 ± 0.10	0.38 ± 0.19

rhombohedral phase with the angles equal to $\theta = 45°, \phi = 0°$; $\theta = 90°, \phi = 45°$, and $\theta = 45°, \phi = 90°$. The values of these minima are equal due to equivalence of the ⟨001⟩, ⟨100⟩, and ⟨010⟩ directions. However, the intersite Cr/Re disorder makes these directions nonequivalent and the corresponding minima differ from each other. The intersite Cr/Re disorder reduces the MAE for the tetragonal and orthorhombic phases and increases it for the rhombohedral phase. The disorder produces also deep local minimum at the ⟨100⟩ direction with a small energy barrier between ⟨001⟩ and ⟨100⟩ directions for the orthorhombic phase.

Figure 11 also presents fitted curves of MAE using the corresponding formulas (1, 2, and 3) with magnetic anisotropy constants K_i presented in Table II. We found that K_1 is the largest magnetic anisotropy constant, as expected, for all phases under consideration. The Cr/Re intersite disorder significantly reduces this constant in the tetragonal and orthorhombic phases and increases it for the rhombohedral one. The same behavior was observed in the case of MAE, as we mentioned above.

We also model the orbital polarization in terms of the Hund's second rule by scaling the corresponding SO term in the Hamiltonian artificially with a constant prefactor. This scaling can be atom dependent, i.e., within each atomic sphere. The outcomes of such constraining calculations for the MAE in the tetragonal phase without intersite Cr/Re disorder are shown in Fig. 12. If we set SO coupling on Cr to zero, the MAE does not change significantly (open magenta circles) in comparison with the initial GGA calculations (full blue circles). On the other hand, when the SO coupling on Re is zero, the MAE almost disappears (open green circles). The scaling of the SO coupling of Re by a factor of 2.0 leads to an increase of the MAE by a factor of 3 confirming a dominant contribution of the SO interaction at the Re site to the large value of MAE in this compound.

It is customary to relate the MAE with the anisotropy of orbital magnetic moment (OMA) ΔM_l [36,102,103]. Figure 13 presents the OMA for the tetragonal, orthorhombic, and rhombohedral phases without the intersite Cr/Re disorder. The OMA are larger at the Re site than at the Cr one. The MAE is

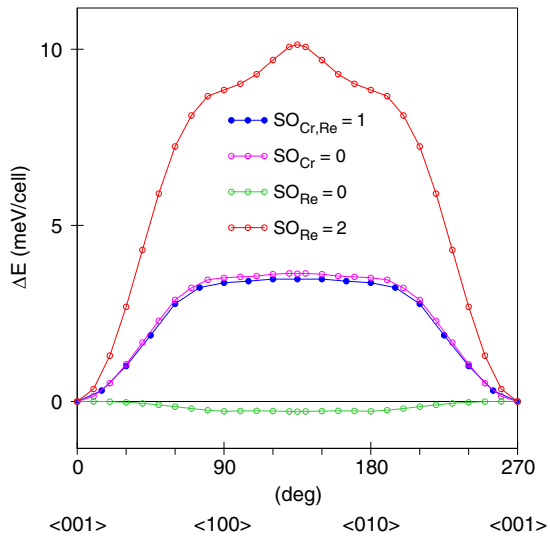

FIG. 12. The effect of scaling the value of SO constant on either Cr or Re atoms on the MAE ΔE in the tetragonal phase of SCRO on BTO (see the text).

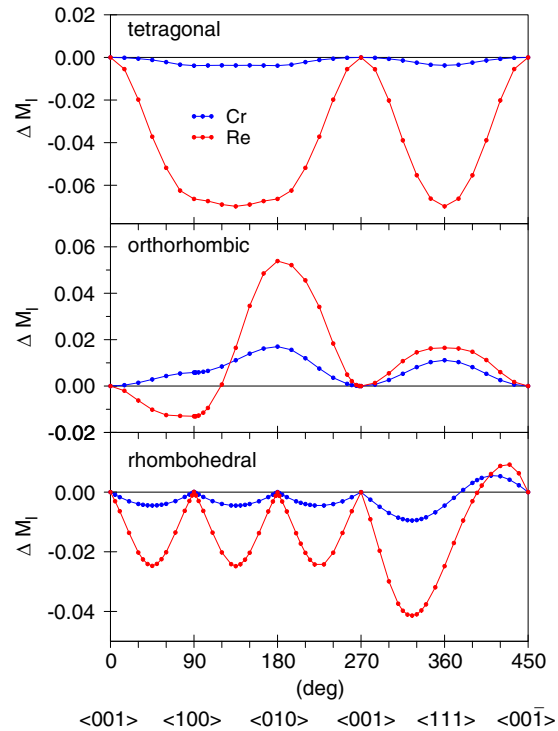

FIG. 13. The OMA (ΔM_l) for the tetragonal (top), orthorhombic (middle), and rhombohedral (bottom) phases without the intersite Cr/Re disorder.

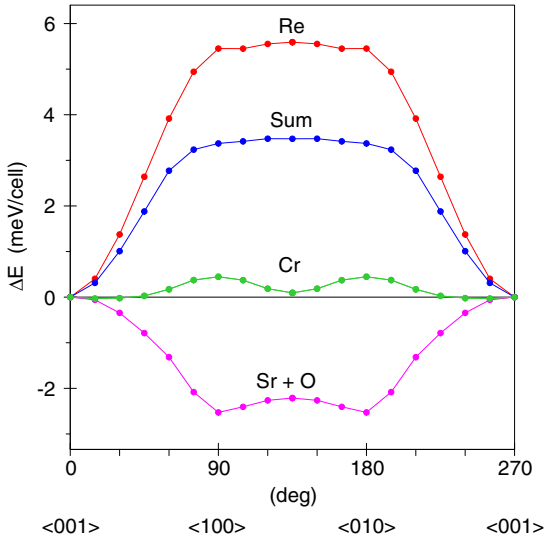

FIG. 14. The partial contribution to the MAE from the Re, Cr, Sr, and O ions for the tetragonal phase of SCRO on BTO without the intersite Cr/Re disorder.

proportional to the OMA through expression $\Delta E \sim \frac{1}{4}\lambda_{SO}\Delta M_l$ [102,103], where λ_{SO} is the SO parameter. The SO constant is $\lambda_{SO} = 0.03$, 0.02, 0.05, and 0.36 eV for Cr, O, Sr, and Re, respectively [104]. Therefore the major contribution to the MAE is expected to be due to the Re site.

We calculated the contributions of each atom to the total energy separately and presented in Fig. 14 the partial contributions to the MAE from the Re, Cr, Sr, and O ions. We found that, indeed, the major contribution comes from the Re site, the corresponding contribution from Cr ions is one order of magnitude smaller. It is interesting to note that the contribution from Sr and O sites is not negligible and even larger than from the Cr one. It can be explained by the fact that SO interaction at the Sr site is stronger than at the Cr site and also the unit cell of SCRO has large number of oxygen ions. Sr and O sites produce negative MAE reducing the total value of MAE in the SCRO on BTO.

Figure 11(d) presents also the MAE ΔE for $[SCRO/BTO]_{1\times1\times1}$ heterostructure. We found that the MAE is increased significantly going from tetragonal SCRO on BTO to the $[SCRO/BTO]_{1\times1\times1}$ heterostructure. The corresponding magnetic anisotropy constants K_1 and K_2 are also increased (see Table II). However, the MAE for $[SCRO/BTO]_{1\times1\times2}$ heterostructure (not shown) became almost two times smaller than the corresponding values for monolayered $[SCRO/BTO]_{1\times1\times1}$ heterostructure, but still a little bit larger in comparison with the SCRO on BTO compound.

V. CONCLUSIONS

The combination of several physical properties such as superconductivity, ferro- and antiferromagnetism, ferroelectricity, or even multiferroicity in artificial heterostructures paves the way to a rich variety of interesting new physics and novel concepts in condensed matter physics. Oxide thin films and their artificial heterostructures are at the forefront of modern materials science due to an enormous progress in oxide thin film technology. On the other hand, they have outstanding physical properties.

In this work, we present a systematic study of the electronic structure and physical properties of SCRO/BTO heterostructures using the fully relativistic spin-polarized Dirac linear muffin-tin orbital band-structure method in the GGA approximation. We found that without SO interactions SCRO double perovskite and all the heterostructures under consideration possess half-metallic character where the only contribution around the Fermi level comes from the minority spins.

The element-specific x-ray absorption spectra and x-ray magnetic circular dichroism at the Ti, Ba, and Re $L_{2,3}$ edges in SCRO and SCRO/BTO heterostructures were investigated theoretically from first principles. The theory describes relatively well the shape and relative intensities of the x-ray absorption and XMCD spectra in the SCRO and BTO. The final-state interaction improves the agreement between the theory and the experiment at the Ti $L_{2,3}$ edges, however, it has a minor influence on the shape of the Ba and Re $L_{2,3}$ XAS spectra.

We investigated theoretically the magnetization, spin, and orbital magnetic moments, as well as the magnetocrystalline anisotropy energy (MAE) in the SCRO on the BTO substrate as a function of the temperature assuming that the finite temperature can be mimicked by the experimental lattice constants corresponding to this temperature. We found that the spin and orbital magnetic moments are monotonic, almost linear functions of temperature but change abruptly at the points of the BTO structural phase transitions. The magnetization M also possesses jumps at the structural phase transitions in agreement with the experiment. The magnetic discontinuity at the structural phase transition is due to the change of the symmetry type and also jump of the c lattice constant, which leads to an abrupt change of interatomic distances and interatomic d-d hybridization. The discontinuity of total magnetic moment is almost one order of magnitude smaller than the experimentally measured one. However, the theoretically calculated temperature dependence of the total magnetic moment with 25% of the Cr/Re disorder (when one of four Cr ions are on Re site and vice versa) is in excellent agreement with the critical amplitude M_0, obtained from the fitting of the experimentally measured magnetization $M(T)$. Such effect of the Cr/Re disorder on the magnetic discontinuity at the structural phase transition is due to the magnetic reconstruction occurring in the SCRO on BTO under the disorder. The major effect comes from the reorientation of the Cr spin moments. The Cr and Re spin sublattices are ordered ferromagntically each and ferrimagnetically to each other in all the crystal structures under consideration for ordered SCRO on BTO. The Cr/Re disorder leads to the ferrimagnetic order for both the Cr and Re sublattices. Moreover, such ferrimagnetic ordering depends on the type of the SCRO crystal structure. In the tetragonal and rhombohedral structures, one Cr ion has spin moment opposite to other Cr moments. It itself significantly reduces the total magnetic moment from 1.396 μ_B to 0.698 μ_B in the tetragonal structure and from 1.390 μ_B to 0.672 μ_B in the rhombohedral structure in agreement with the experiment. In the case of the orthorhombic crystal structure, two Cr ions have spin moments opposite to the other two Cr moments. This almost antiferromagnetic (AF) ordering of Cr ions produces a very small average spin moment

at the Cr sublattice and the total magnetic moment is derived by the spin and orbital magnetic moments at the Re sites. Such reconstruction produces a jump in the total magnetic moment of 0.299 μ_B at the tetragonal/orthorhombic phase transition for the Cr/Re disordered system in comparison with only 0.020 μ_B for the ordered SCRO on BTO. The orientation of the Cr spin magnetic moments plays a major role for the significant increase of magnetic discontinuity at the structural phase transition. However, one has to take into account also the spin and orbital magnetic moments at the Re sites to obtain the precise values of the total magnetic moments. To achieve an agreement with the experiment, we have to assume AF ordering in Cr sites in the orthorhombic crystal structure. Although the ferrimagnetic order with one Cr spin moment opposite to the other three ones is slightly lower in total energy than the AF order, it produces a smaller jump in comparison with the experiment (however, still larger than in the case of ordered structure). One has to mention that SCRO on BTO system is far from the thermodynamic equilibrium. The SCRO film is in large strain due to the pulsed laser deposition specimen preparation and relatively large mismatch between SCRO and BTO lattice constants. Therefore the total energy analysis in this case can not be valid. One of the reasons of the AF ordering of Cr spin moments might be the twinning effect of the BTO susbstrate in the orthorhombic phase, which is absent for the two other phases.

We found that the easy axis of magnetization for the tetragonal phase is along the $\langle 001 \rangle$ direction for both ordered and disordered structures. The ordered orthorhombic phase also has the easy axis of magnetization along the $\langle 001 \rangle$ direction, however, intersite Cr/Re disorder changes the easy axis of magnetization approximately to the $\langle 00\bar{1} \rangle$ direction. The rhombohedral phase has the easy axis of magnetization approximately along the $\langle 11\bar{1} \rangle$ direction. These conclusions are in agreement with the measurements of the magnetization versus external magnetic field in the SCRO on BTO measured by Czeschka *et al.* [25].

The MAE is proportional to the SO parameter λ_{SO} and the anisotropy of orbital magnetic moment. The OMA is larger at the Re site than at the Cr one, besides, λ_{SO} is one order of magnitude larger for 5*d* Re than 3*d* Cr. Therefore one would expect the dominant contribution to the MAE from the Re site in SCRO on BTO. The direct calculations of the contributions of each atom to the total energy confirm it. We also found that the contributions from Sr and O sites are not negligible and even larger than from the Cr one. It can be explained by the fact that SO interaction at the Sr site is stronger than at the Cr site, and also the unit cell of SCRO has a large number of oxygen ions. Sr and O sites produce negative MAE reducing the total value of MAE in the SCRO on BTO.

The MAE ΔE is increased significantly going from tetragonal SCRO on BTO to the $[\mathrm{SCRO/BTO}]_{1\times1\times1}$ heterostructure. The corresponding magnetic anisotropy constants K_1 and K_2 are also increased. However, the MAE for $[\mathrm{SCRO/BTO}]_{1\times1\times2}$ heterostructure becomes almost two times smaller than the corresponding value for monolayered $[\mathrm{SCRO/BTO}]_{1\times1\times1}$ heterostructure, but still a little bit larger in comparison with the pure tetragonal SCRO on BTO compound.

Artificial oxide heterostructures are particularly promising for the realization of materials with improved and new functionalities and novel device concepts. Due to the complexity of the involved oxide materials, the rich variety of physics is far from being understood and needs further detailed studies. Moreover, intermixing of the different atomic species deposited in multilayer structures plays an important role and might influence or even dominate the overall physical properties. Therefore a careful investigation of the electronic structure, optical, and element-specific XMCD properties of artificially constructed material systems is highly desirable.

ACKNOWLEDGMENTS

V.N.A. gratefully acknowledges the hospitality at the Faculty of Mathematics and Informatics of the University of Bialystok and Max-Planck Institut für Mikrostrukturphysik during his stay there. Calculations were partially carried out at the Computing Center of University of Bialystok.

[1] I. E. Dzyaloshinskii, Sov. Phys.-JETP **10**, 628 (1959).
[2] D. N. Astrov, Sov. Phys.-JETP **11**, 708 (1960).
[3] H. Schmid, Ferroelectrics **162**, 317 (1994).
[4] T. Kimura, T. Goto, K. Thizaka, T. Arima, and Y. Tokura, Nature (London) **426**, 55 (2003).
[5] T. Lottermoser, T. Lonkai, U. Amann, D. Hohlwein, J. Ihringer, and M. Fiebig, Nature (London) **430**, 541 (2003).
[6] T. Lottermosera, H. Yamada, J. Matsuno, T. Arima, M. Kawasaki, and Y. Tokura, J. Magn. Magn. Mater. **310**, 2204 (2007).
[7] J. T. Heron, D. G. Schlom, and R. Ramesh, Appl. Phys. Rev. **1**, 021303 (2014).
[8] C.-W. Nan, M.-I. Bichurin, S. Dong, D. Viehland, and G. Srinivasan, J. Appl. Phys. **103**, 031101 (2008).
[9] N. A. Hill, J. Phys. Chem. B **104**, 6694 (2000).
[10] C. W. Nan, G. Liu, Y. Lin, and H. Chen, Phys. Rev. Lett. **94**, 197203 (2005).
[11] P. Hajra, R. Maiti, and D. Chakravorty, Trans. Ind. Ceram. Soc. **70**, 53 (2011).
[12] R. V. Chopdekar and Y. Suzuki, Appl. Phys. Lett. **89**, 182506 (2006).
[13] M. K. Lee, T. K. Nath, C. B. Eom, M. C. Smoak, and F. Tsui, Appl. Phys. Lett. **77**, 3547 (2000).
[14] D. Dale, A. Fleet, J. D. Brock, and Y. Suzuki, Appl. Phys. Lett. **82**, 3725 (2003).
[15] W. Eerenstein, M. Wiora, J. L. Prieto, J. F. Scott, and N. D. Mathur, Nat. Mater. **6**, 348 (2007).
[16] H. F. Tian, T. L. Qu, L. B. Luo, J. J. Yang, S. M. Guo, H. Y. Zhang, Y. G. Zhao, and J. Q. Li, Appl. Phys. Lett. **92**, 063507 (2008).
[17] C. A. F. Vaz, J. Hoffman, A.-B. Posadas, and C. H. Ahn, Appl. Phys. Lett. **94**, 022504 (2009).
[18] K. I. Kobayashi, T. Kimura, H. Sawada, K. Terakura, and Y. Tokura, Nature (London) **395**, 677 (1998).

[19] H. Kato, T. Okuda, Y. Okimoto, Y. Tomioka, K. Oikawa, T. Kamiyama, and Y. Tokura, Phys. Rev. B **69**, 184412 (2004).

[20] J. M. D. Coey, Adv. Phys. **48**, 167 (1999).

[21] D. Serrate, J. M. D. Teresa, and M. R. Ibarra, J. Phys.: Condens. Matter **19**, 023201 (2007).

[22] J. B. Philipp, P. Majewski, L. Alff, A. Erb, R. Gross, T. Graf, M. S. Brandt, J. Simon, T. Walther, W. Mader *et al.*, Phys. Rev. B **68**, 144431 (2003).

[23] H. Kato, T. Okuda, Y. Okimoto, Y. Tomioka, K. Oikawa, T. Kamiyama, and Y. Tokura, Phys. Rev. B **65**, 144404 (2002).

[24] Y. Krockenberger, K. Mogare, M. Reehuis, M. Tovar, M. Jansen, G. Vaitheeswaran, V. Kanchana, F. Bultmark, A. Delin, F. Wilhelm *et al.*, Phys. Rev. B **75**, 020404(R) (2007).

[25] F. D. Czeschka, S. Geprags, M. Opel, S. T. B. Goennenwein, and R. Gross, Appl. Phys. Lett. **95**, 062508 (2009).

[26] M. Opel, S. Gergäs, E. P. Menzel, A. Nielsen, D. Reisinger, K.-W. Nielsen, A. Brandlmaier, F. D. Czeschka, M. Althammer, M. Weiler *et al.*, Phys. Status Solidi A **208**, 232 (2011).

[27] C. Hirjibehedin, C. Lin, A. Otte, M. Ternes, C. Lutz, and B. Jones, Science **317**, 1199 (2007).

[28] H. Brooks, Phys. Rev. **58**, 909 (1940).

[29] G. C. Fletcher, Proc. R. Soc. London, Ser. A **67**, 505 (1954).

[30] J. Trygg, B. Johansson, O. Eriksson, and J. M. Wills, Phys. Rev. Lett. **75**, 2871 (1995).

[31] S. V. Halilov, A. Y. Perlov, P. M. Oppeneer, A. N. Yaresko, and V. N. Antonov, Phys. Rev. B **57**, 9557 (1998).

[32] P. Ravindran, A. Delin, P. James, B. Johansson, J. M. Wills, R. Ahuja, and O. Eriksson, Phys. Rev. B **59**, 15680 (1999).

[33] G. H. O. Daalderop, P. J. Kelly, and M. F. H. Schuurmans, Phys. Rev. B **41**, 11919 (1990).

[34] D.-S. Wang, R. Wu, and A. J. Freeman, Phys. Rev. Lett. **70**, 869 (1993).

[35] V. N. Antonov, B. N. Harmon, A. N. Yaresko, L. V. Bekenov, and A. P. Shpak, Phys. Rev. B **73**, 094445 (2006).

[36] V. P. Antropov, V. N. Antonov, L. V. Bekenov, A. Kutepov, and G. Kotliar, Phys. Rev. B **90**, 054404 (2014).

[37] V. P. Antropov and V. N. Antonov, Phys. Rev. B **90**, 094406 (2014).

[38] L. D. Landau, E. M. Lifshitz, and L. P. Pitaevski, *Electrodynamics of Continuous Media*, Course of Theoretical Physics Vol. 8, 2nd ed. (Elsvier, 2004).

[39] R. Skomski, *Simple Models of Magnetism* (Oxford University Press, Oxford, 2008).

[40] A. Schrön, C. Rödl, and F. Bechstedt, Phys. Rev. B **86**, 115134 (2012).

[41] L. A. Shebanov, Phys. Status Solidi A **65**, 321 (1981).

[42] H. F. Kay and P. Vousden, Philos. Mag. **40**, 1019 (1949).

[43] V. N. Antonov, M. Galli, F. Marabelli, A. N. Yaresko, A. Y. Perlov, and E. Bauer, Phys. Rev. B **62**, 1742 (2000).

[44] V. N. Antonov, B. N. Harmon, and A. N. Yaresko, Phys. Rev. B **63**, 205112 (2001).

[45] V. N. Antonov, O. Jepsen, A. N. Yaresko, and A. P. Shpak, J. Appl. Phys. **100**, 043711 (2006).

[46] V. N. Antonov, B. N. Harmon, A. N. Yaresko, and A. P. Shpak, Phys. Rev. B **75**, 184422 (2007).

[47] L. Uba, S. Uba, L. P. Germash, L. V. Bekenov, and V. N. Antonov, Phys. Rev. B **85**, 125124 (2012).

[48] O. K. Andersen, Phys. Rev. B **12**, 3060 (1975).

[49] A. Y. Perlov, A. N. Yaresko, and V. N. Antonov, PY-LMTO, A Spin-polarized Relativistic Linear Muffin-tin Orbitals Package for Electronic Structure Calculations (unpublished).

[50] V. V. Nemoshkalenko, A. E. Krasovskii, V. N. Antonov, V. N. Antonov, U. Fleck, H. Wonn, and P. Ziesche, Phys. Status Solidi B **120**, 283 (1983).

[51] J. P. Perdew and Y. Wang, Phys. Rev. B **45**, 13244 (1992).

[52] J. P. Perdew, K. Burke, and M. Ernzerhof, Phys. Rev. Lett. **77**, 3865 (1996).

[53] P. E. Blöchl, O. Jepsen, and O. K. Andersen, Phys. Rev. B **49**, 16223 (1994).

[54] P. E. Blöchl, Phys. Rev. B **50**, 17953 (1994).

[55] G. Kresse and D. Joubert, Phys. Rev. B **59**, 1758 (1999).

[56] K. Lie, R. Hoier, and R. Brydson, Phys. Rev. B **61**, 1786 (2000).

[57] S.-D. Mo and W. Y. Ching, Phys. Rev. B **62**, 7901 (2000).

[58] S.-D. Mo and W. Y. Ching, Appl. Phys. Lett. **78**, 3809 (2001).

[59] Y.-N. Xu, Y. Chen, S.-D. Mo, and W. Y. Ching, Phys. Rev. B **65**, 235105 (2002).

[60] W.-Y. Ching, S.-D. Mo, and Y. Chen, J. Am. Ceram. Soc. **85**, 11 (2002).

[61] T. Mizoguchi, I. Tanaka, S. Yoshioka, M. Kunisu, T. Yamamoto, and W. Y. Ching, Phys. Rev. B **70**, 045103 (2004).

[62] A. R. Mackintosh and O. K. Andersen, in *Electrons at the Fermi Surface*, edited by M. Springford (Cambridge University Press, Cambridge, 1980), pp. 149–224.

[63] B. C. Jeon, C. H. Kim, S. J. Moon, W. S. Choi, H. Jeong, Y. S. Lee, J. Yu, C. J. Won, J. H. Jung, N. Hur *et al.*, J. Phys.: Condens. Matter **22**, 345602 (2010).

[64] G. G. Scott, J. Phys. Soc. Jpn. **17**, 372 (1962).

[65] W. Marshall and S. W. Lovsey, *Theory of Thermal Neutron Scattering* (Oxford University Press, Oxford, 1971).

[66] M. Blume, J. Appl. Phys. **57**, 3615 (1985).

[67] B. T. Thole, P. Carra, F. Sette, and G. van der Laan, Phys. Rev. Lett. **68**, 1943 (1992).

[68] P. Carra, B. T. Thole, M. Altarelli, and X. Wang, Phys. Rev. Lett. **70**, 694 (1993).

[69] H. Das, M. D. Raychaudhury, and T. Saha-Dasgupta, Appl. Phys. Lett. **92**, 201912 (2008).

[70] J. Wang, N. Zu, Y. Wang, and Z. Wu, Phys. Status Solidi **7**, 583 (2013).

[71] P. Majewski, S. Geprags, O. Sanganas, M. Opel, R. Gross, F. Wilhelm, A. Rogalev, and L. Alff, Appl. Phys. Lett. **87**, 202503 (2005).

[72] G. Vaitheeswaran, V. Kanchana, M. Alouani, and A. Delin, Europhys. Lett. **84**, 47005 (2008).

[73] H. Ebert, Rep. Prog. Phys. **59**, 1665 (1996).

[74] V. Antonov, B. Harmon, and A. Yaresko, *Electronic Structure and Magneto-Optical Properties of Solids* (Kluwer, Dordrecht, 2004).

[75] T. Böske, W. Clemens, C. Carbone, and W. Eberhardt, Phys. Rev. B **49**, 4003 (1994).

[76] C. T. Chen, Y. U. Idzerda, H.-J. Lin, N. V. Smith, G. Meigs, E. Chaban, G. H. Ho, E. Pellegrin, and F. Sette, Phys. Rev. Lett. **75**, 152 (1995).

[77] G. Gupta, T. Nautiyal, and S. Auluck, Phys. Rev. B **69**, 052101 (2004).

[78] S. H. Wemple, Phys. Rev. B **2**, 2679 (1970).

[79] D. Bagayoko, G. L. Zhao, J. D. Fan, and J. T. Wang, J. Phys.: Condens. Matter **10**, 5645 (1998).

[80] S. Saha, T. P. Sinha, and A. Mookerjee, Phys. Rev. B **62**, 8828 (2000).
[81] J. Zhang, A. Visinoiu, F. Heyroth, F. Syrowatka, M. Alexe, D. Hesse, and H. S. Leipner, Phys. Rev. B **71**, 064108 (2005).
[82] A. Chasse, S. Borek, K.-M. Schindler, M. Trautmann, M. Huth, F. Steudel, L. Makhova, J. Gräfe, and R. Denecke, Phys. Rev. B **84**, 195135 (2011).
[83] G. Liu, Y. Wang, B. Zou, W. Liang, N. M. Alford, D. W. McComb, and P. K. Petrov, J. Phys. Chem. C **120**, 16681 (2016).
[84] A. S. Sefat, G. Amow, M. Y. Wu, G. A. Botton, and J. E. Greedan, J. Solid State Chem. **178**, 1008 (2005).
[85] J. Zaanen, G. A. Sawatzky, J. Fink, W. Speier, and J. C. Fuggle, Phys. Rev. B **32**, 4905 (1985).
[86] J. Schwitalla and H. Ebert, Phys. Rev. Lett. **80**, 4586 (1998).
[87] P. Krüger and C. R. Natoli, Phys. Rev. B **70**, 245120 (2004).
[88] A. L. Ankudinov, A. I. Nesvizhskii, and J. J. Rehr, Phys. Rev. B **67**, 115120 (2003).
[89] K. Yoshii, I. Jarrige, C. Suzuki, D. Matsumura, Y. Nishihata, Y. Yoneda, T. Fukuda, K. Tamura, Y. Ito, T. Mukoyama *et al.*, J. Phys. Chem. Solids **73**, 1106 (2012).
[90] A. J. Hauser, J. M. Lucy, M. W. Gaultois, M. R. Ball, J. R. Soliz, Y. Choi, O. D. Restrepo, W. Windl, J. W. Freeland, D. Haskel *et al.*, Phys. Rev. B **89**, 180402(R) (2014).
[91] K. Asokan, J. C. Jan, J. W. Chiou, W. F. Pong, P. K. Tseng, and I. N. Lin, J. Synchrotron Radiat. **8**, 839 (2001).
[92] K. Asokan, J. C. Jan, J. W. Chiou, W. F. Pong, M.-H. Tsai, H. L. Shih, H. Y. Chen, H. C. Hsueh, C. C. Chuang, Y. K. Chang *et al.*, J. Phys.: Condens. Matter **13**, 11087 (2001).
[93] Y.-H. Tang, M.-H. Tsai, J. Jan, and W. Pong, Chin. J. Phys. **41**, 167 (2003).
[94] M. Hidaka, N. Tokiwa, S. Takahashi, J.-Y. Choi, and J. M. Lee, Phys. Status Solidi B **241**, 1058 (2004).
[95] K. Yoshii, Y. Yoneda, I. Jarrige, T. Fukuda, Y. Nishihata, C. Suzuki, Y. Ito, T. Terashima, S. Yoshikado, and S. Fukushima, J. Phys. Chem. Solids **75**, 339 (2014).
[96] R. E. Cohen and H. Krakauer, Phys. Rev. B **42**, 6416 (1990).
[97] F. M. F. Groot, Physica B **208–209**, 15 (1995).
[98] A. Dhahri, M. Jemmali, E. Dhahri, and E. Hlil, J. Alloys Comp. **631**, 350 (2015).
[99] A. Dhahri, M. Jemmali, M. Hussein, E. Dhahri, A. Koumina, and E. Hlil, J. Alloys Comp. **618**, 788 (2015).
[100] D. Kim, B. Revaz, B. L. Zink, F. Hellman, J. J. Rhyne, and J. F. Mitchell, Phys. Rev. Lett. **89**, 227202 (2002).
[101] G. H. Kwei, A. C. Lawson, S. J. L. Billinge, and S.-W. Cheng, J. Phys. Chem. **97**, 2368 (1993).
[102] K. Yosida, A. Okiji, and S. Chikazumi, Prog. Theor. Phys. **33**, 559 (1965).
[103] M. Cinal, D. M. Edwards, and J. Mathon, Phys. Rev. B **50**, 3754 (1994).
[104] M. Montalti, A. Credi, L. Prodi, and M. T. Gandolfi, in *Handbook of Photochemistry*, edited by N. J. Turro (Taylor and Francis Group, Boca Raton, FL, 2006), p. 629.